Article

Monolithic silicon for high spatiotemporal translational photostimulation

https://doi.org/10.1038/s41586-024-07016-9

Received: 10 May 2023

Accepted: 2 January 2024

Published online: 21 February 2024

Check for updates

Pengju Li[1], Jing Zhang[2], Hidenori Hayashi[3], Jiping Yue[4], Wen Li[4], Chuanwang Yang[2], Changxu Sun[1], Jiuyun Shi[4], Judah Huberman-Shlaes[4], Narutoshi Hibino[3]✉ & Bozhi Tian[2,4,5]✉

Electrode-based electrical stimulation underpins several clinical bioelectronic devices, including deep-brain stimulators[1,2] and cardiac pacemakers[3]. However, leadless multisite stimulation is constrained by the technical difficulties and spatial-access limitations of electrode arrays. Optogenetics offers optically controlled random access with high spatiotemporal capabilities, but clinical translation poses challenges[4–6]. Here we show tunable spatiotemporal photostimulation of cardiac systems using a non-genetic platform based on semiconductor-enabled biomodulation interfaces. Through spatiotemporal profiling of photoelectrochemical currents, we assess the magnitude, precision, accuracy and resolution of photostimulation in four leadless silicon-based monolithic photoelectrochemical devices. We demonstrate the optoelectronic capabilities of the devices through optical overdrive pacing of cultured cardiomyocytes (CMs) targeting several regions and spatial extents, isolated rat hearts in a Langendorff apparatus, in vivo rat hearts in an ischaemia model and an in vivo mouse heart model with transthoracic optical pacing. We also perform the first, to our knowledge, optical override pacing and multisite pacing of a pig heart in vivo. Our systems are readily adaptable for minimally invasive clinical procedures using our custom endoscopic delivery device, with which we demonstrate closed-thoracic operations and endoscopic optical stimulation. Our results indicate the clinical potential of the leadless, lightweight and multisite photostimulation platform as a pacemaker in cardiac resynchronization therapy (CRT), in which lead-placement complications are common.

Leadless flexible bioelectronics[7–9] that modulate bioelectrical signalling in a manner similar to the body's own regulatory mechanisms (Supplementary Fig. 1, left) can offer new treatment paths for neurodegenerative[10,11] and cardiac diseases[3,12]. Optically mediated genetic systems offer high spatiotemporal resolution and tunability, with random-access capabilities for cellular and tissue stimulation[13,14]. For clinical translation, recent non-genetic photodiode-based optoelectronic devices, which convert light into electrical currents, efficiently modulate cells and tissues at optical-power levels comparable with those used in optogenetics[15–18]. Micropatterned pixelated optoelectrodes that enable localized stimulation with high resolution demonstrate great potential for retinal prosthesis[19–22]. Nonetheless, the translational potential of monolithic photoelectrochemical devices that facilitate multisite biostimulation hinges on clear characterization of the photostimulation response profile, in terms of precision, accuracy and resolution (Fig. 1a, left).

At the cellular level, individual neurons feature both current sources and sinks, resulting in a globally charge-balanced network with locally heterogeneous extracellular potentials in the form of dipoles and even n-poles[23] (Supplementary Fig. 1, middle). Although similar effects have been reported in faceted crystals[24], heterodimers[25] and other microfabricated systems with either dopant or voltage control, random-access and leadless dipole formation on a monolithic surface has not been clearly demonstrated (Fig. 1a, middle). At the molecular level, neuronal excitation can involve fast sodium inward currents, slow calcium inward currents and fast or slow potassium currents (Supplementary Fig. 1, right). These ionic currents are analogous to steady faradaic currents and fast capacitive cathodic and anodic currents in photoelectrochemical systems (Fig. 1a, right). Achievement of both paves the way to leadless photoelectrochemical systems for bioelectrical modulation.

Photogenerated carriers and their dynamics in photoelectrochemical materials play a crucial role in shaping photocurrent distribution profiles. In solar-energy harvesting, single-crystalline silicon (Si) or perovskites[26] are usually preferred over their polycrystalline counterparts. Elimination of grain-boundary recombination leads to increased carrier lifetimes and, consequently, enhanced collection efficiency[27,28]. By contrast, high spatiotemporal photocurrent generation benefits from tightly confined carrier diffusion (Fig. 1a, left). In this study, we systematically assess the spatiotemporal profiles of photoelectrochemical current generation and dynamics in four variations of

[1]Pritzker School of Molecular Engineering, The University of Chicago, Chicago, IL, USA. [2]The James Franck Institute, The University of Chicago, Chicago, IL, USA. [3]Section of Cardiac Surgery, Department of Surgery, The University of Chicago, Chicago, IL, USA. [4]Department of Chemistry, The University of Chicago, Chicago, IL, USA. [5]Institute for Biophysical Dynamics, The University of Chicago, Chicago, IL, USA. ✉e-mail: nhibino@bsd.uchicago.edu; btian@uchicago.edu

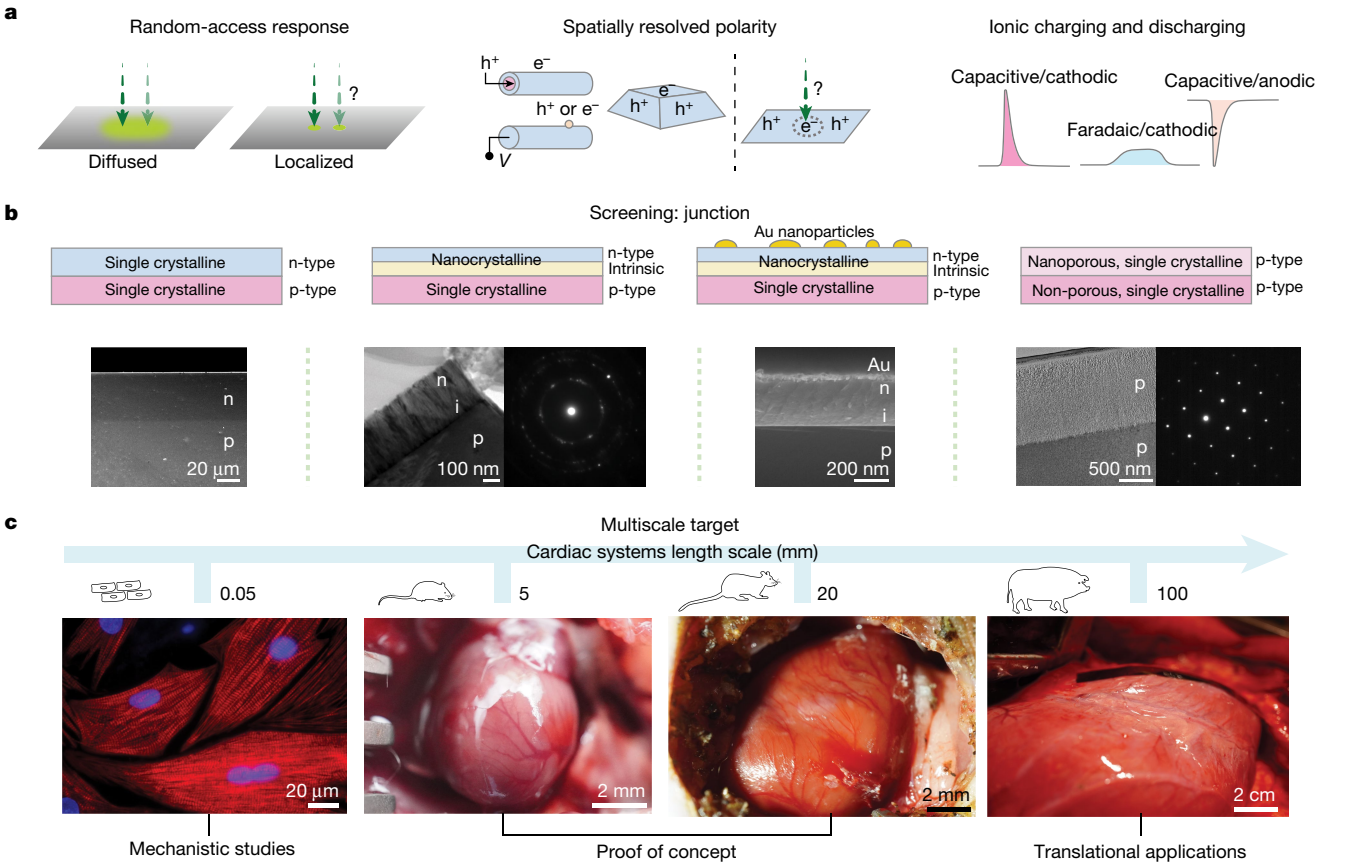

Fig. 1 | Design concepts for monolithic photoelectrochemical devices with high-spatiotemporal-resolution photoresponse. a, Underexplored photoelectrochemical properties can guide better design of bioelectrical modulation with high spatiotemporal resolution. Left, high-resolution and localized photostimulation for random-access photocurrent generation. Middle, optically controlled and spatially resolved polarity enables charge balance, allowing cathodic and anodic processes to occur on the same material surface. Right, temporal photoresponse profile comprising fast cathodic, slow faradaic and fast anodic processes. e^- and h^+ represent electrons and holes, respectively; V is applied voltage. **b**, Junction design and screening for development of monolithic photoelectrochemical devices. Scanning electron microscopy images, transmission electron microscopy images and diffraction patterns show representative cross-sections of the four semiconductor-junction structures. Images shown are representatives from $N = 3$ devices. **c**, Multiscale cardiac systems used in this study enable mechanistic studies and proof-of-concept demonstrations and highlight translational potential. Cardiac systems include neonatal and adult CMs, mouse and rat heart models and pig heart models.

monolithic Si-based photoelectrochemical devices (Fig. 1b) to delineate multisite photostimulation capability in biological systems. Their capacity for multiscale configurations (Supplementary Fig. 2) also suggests new opportunities in biological interfaces (Supplementary Fig. 3). We demonstrate multiscale spatiotemporal cardiac modulation (Fig. 1c and Supplementary Table 1) in in vitro-cultured rat CMs and ex vivo and in vivo rat heart models. We perform a tissue-penetrating photostimulation experiment in a mouse heart in vivo to illustrate non-invasive stimulation. We demonstrate reliable multisite cardiac control with millisecond-duration light pulses in a live pig heart experiment under clinical open-thoracic conditions. Finally, we demonstrate closed-thoracic pig heart stimulation using a custom endoscopic operation system, highlighting translational potential. Beyond biointerface research, the capacity for spatial manipulation of photoelectrochemical current polarity on a monolithic semiconductor surface has wide-ranging implications in energy science and catalysis.

Spatiotemporal photocurrent profiling

We introduce spatiotemporal photoelectrochemical device profiling (Fig. 2, Extended Data Fig. 4 and Supplementary Videos 1–4) as a new approach to assess spatiotemporal capability in semiconductor–saline systems. Following focused-spot illumination, photogenerated carriers in semiconductor–electrolyte systems undergo a series of processes: (1) photocarrier generation and separation; (2) solid-state carrier diffusion; (3) electrochemical processes at the semiconductor–electrolyte interface; and (4) ion diffusion owing to concentration difference (Supplementary Fig. 4). The last two processes involve aqueous-state chemical dynamics on the device and can be characterized with millisecond and microsecond temporal resolution using our customized patch-clamp technique.

We fabricated four Si-based photodiode devices with distinct configurations: single-crystalline p-n Si (sPN-Si); p-i-n type Si (PIN-Si); Au nanoparticle-decorated p-i-n Si (PIN-Si (Au)); and a porosity-based heterojunction (Por-Si). Figure 2a illustrates the electron (cathodic) and hole (anodic) diffusion processes from the light beam centre for the different configurations. The governing equation for effective carrier diffusion length (L_e) and effective carrier lifetime (τ_e) for the photogenerated electrons can be approximated as equations (1) and (2):

$$\text{Carrier diffusion length}: L_e = \sqrt{D\tau_e} \quad (1)$$

$$\text{Effective carrier lifetime}: \frac{1}{\tau_e} \sim \frac{1}{\tau_b} + \frac{1}{\tau_{GB}} + \frac{1}{\tau_s} + \frac{1}{\tau_a} \quad (2)$$

in which D represents the diffusion coefficient, and τ_b, τ_{GB}, τ_s and τ_a refer to the contribution from bulk, grain-boundary, surface and Auger recombination, respectively, to carrier lifetime. The charge-returning

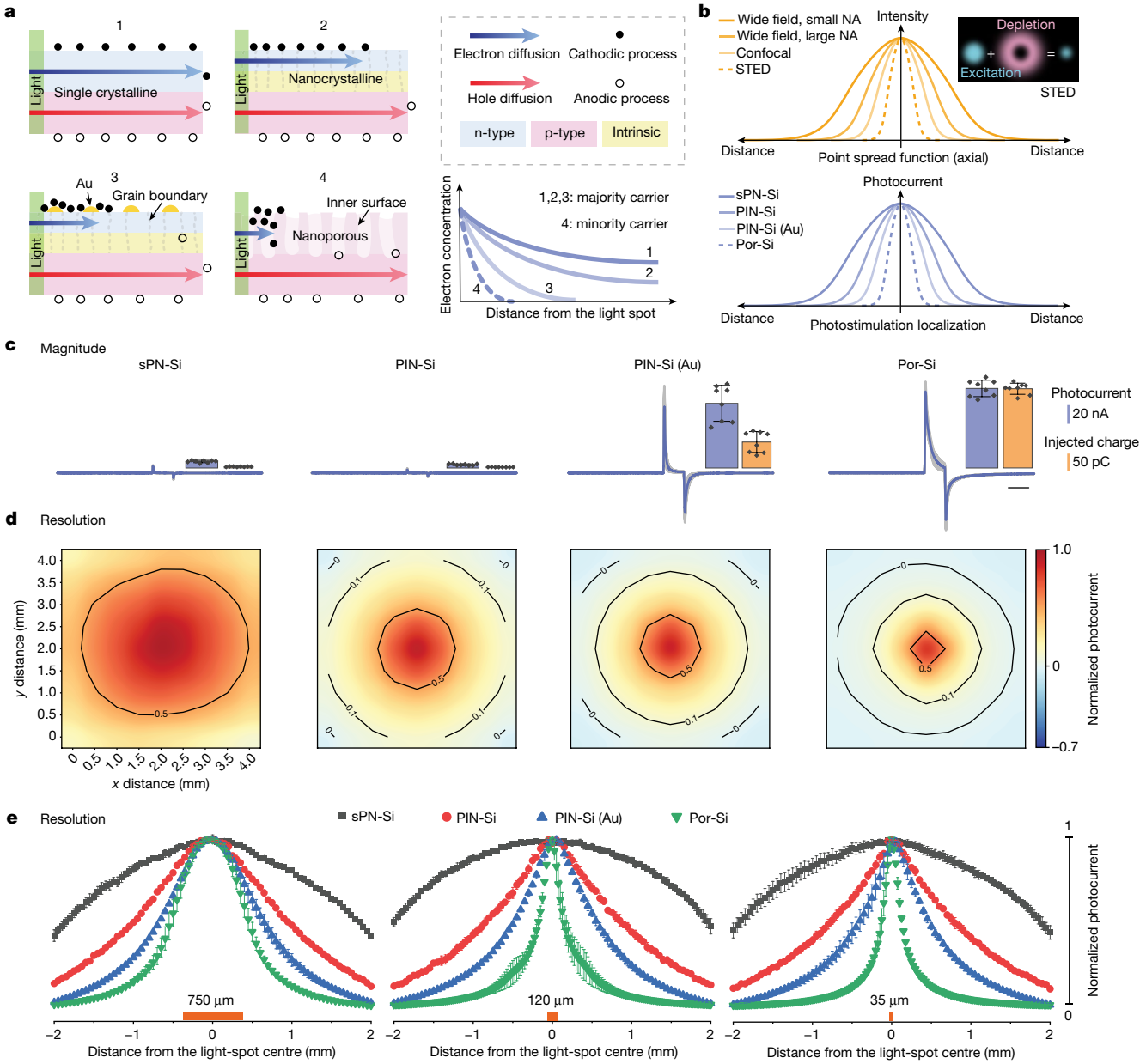

Fig. 2 | Spatial profiles of device photoelectrochemical responses. a, Four distinct semiconductor configurations and their predicted carrier diffusion distance under localized illumination. In sPN-Si, PIN-Si and PIN-Si (Au), the cathodic process is dominated by electrons as majority carriers. In Por-Si, the cathodic process involves minority carriers. 1, 2, 3, 4 denote sPN-Si, PIN-Si, PIN-Si (Au) and Por-Si, respectively. **b**, Analogy between photocurrent-intensity distribution and light-intensity distribution (optical microscopy) illustrates the spatial resolution improvements of imaging (upper panel) or stimulation (lower panel). Stimulated emission depletion (STED) microscopy and Por-Si-based photostimulation represent two depletion-based approaches for improving the resolution. NA, numerical aperture. **c**, Comparison of photocurrent magnitudes across four Si-based devices. Blue traces represent the averaged photocurrents from $N = 8$ independent devices and the overlaid grey traces illustrate individual device measurements. The accompanying bar graph shows peak photocurrent values (in blue) and integrated charge injections (in orange). Bar graphs are expressed as mean ± s.d. Scale bar, 10 ms. **d**, Resolution is determined by mapping the normalized photocurrent against the illumination centre. **e**, Photocurrent profiles of the four Si-based devices with various spot sizes. Higher resolution signifies more localized photostimulation and a tunable stimulation zone controlled by the light-spot size. Data are expressed as mean ± s.d. from measurements on $N = 3$ devices.

process, that is, the anodic current, from the Si-based devices in saline will show different spatiotemporal profiles and may help confine the cathodic domains by means of 'depletion' (Fig. 2b), which is reminiscent of stimulated emission depletion microscopy in its potential to attain elevated spatial resolutions (Fig. 2b, upper panel).

The cathodic processes in the first three devices are enabled by majority-carrier diffusion in the n-type Si top layers. As majority carriers have intrinsically longer diffusion lengths, they would yield more delocalized photoelectrochemical reactions (Fig. 2a). In Por-Si (Supplementary Fig. 5), electrons diffuse as minority carriers in the p-type nanoporous Si layer; solid-state diffusion length could be reduced further by the nanoporous structures and large surface areas (that is, smaller terms such as τ_b and τ_s). Considering also the potential solution-phase 'depletion' from the anodic process (Fig. 2b), we propose that Por-Si would offer the best cathodic photostimulation localization and, consequently, the tunability of high-spatial-resolution photocurrent.

The absolute photocurrent magnitude under identical illumination and recording conditions (Fig. 2c) follows the sequence

Por-Si > PIN-Si (Au) > sPN-Si > PIN-Si. Notably, nitric acid and plasma treatment resulted in improved photocurrent generation in this version of Por-Si compared with the previously reported version[17] (Supplementary Fig. 6), attributed to increased surface activation and oxidation states (energy-dispersive X-ray spectroscopy and X-ray photoelectron spectroscopy in Supplementary Fig. 7). In photostability assessments, all four devices maintained more than 85% of their initial photocurrent values after 1,000 cycles of illumination with an intensity of 45 mW mm^{-2} (Supplementary Fig. 8).

We assessed device precision, accuracy and resolution of photostimulation by spatially mapping the maximum (photocathodic) or minimum (photoanodic) photocurrent peaks during the ON stage of illumination across the Si surfaces (see Methods; Supplementary Fig. 9). In precision tests (Extended Data Fig. 1), PIN-Si and Por-Si showed minimal standard deviation (s.d.) in their recorded photoelectrochemical currents, 0.043 and 0.026, respectively. PIN-Si (Au), with non-evenly decorated nanoparticles (Supplementary Fig. 10), and sPN-Si exhibited reduced uniformity, with s.d. values of 0.193 and 0.145, respectively. In accuracy tests (Extended Data Fig. 2), PIN-Si, PIN-Si (Au) and Por-Si maintained alignment between the photoelectrochemical current and optical excitation centres for both edge and corner illumination, whereas sPN-Si exhibited errors of 75% and 100%, respectively. Under photocurrent mapping (Fig. 2d), as well as profiling with varying light-spot sizes, ranging from 750 µm to 35 µm (Fig. 2e and Supplementary Fig. 9c), Por-Si exhibited the best photocurrent localization and most pronounced change in photoelectrochemical current full width at half maximum (FWHM), signifying a higher degree of optically tunable resolution (Extended Data Fig. 3). Point measurements in photocurrent precision and resolution mapping are shown in the supporting information (Supplementary Figs. 11–22).

Spatiotemporal maps for Por-Si (Extended Data Fig. 4 and Supplementary Video 4) show that, at about 0.3 ms after illumination, a cathodic charge injection emerges, followed by cathodic current diffusion until roughly 0.7 ms (Supplementary Fig. 4, steps 3 and 4). Analogously, a polarity reversal from the area of the localized photocurrent was observed approximately 0.3 ms following the cessation of light, signifying discharging dynamics. Spatiotemporal profiles for PIN-Si (Au) and PIN-Si showed similar photocurrent bipolarity dynamics with less localized cathodic domains and sPN-Si showed unipolar cathodic current profile on the device surface (Supplementary Fig. 23 and Supplementary Videos 1–3).

The observation of opposite polarities on the same surface of the Por-Si device (Extended Data Fig. 4a) implies that the photogenerated holes (majority carriers in p-type Si) diffuse further than the electrons, facilitating anodic charge injection through the peripheral porous region (Supplementary Fig. 24). Therefore, the device could function without a separate return electrode. We discerned a consistent peak current independent of illumination duration with Por-Si, underscoring the potential for high-temporal-precision photostimulation (Supplementary Fig. 25a,b). Moreover, the observed biphasic waveforms suggest an inherent charge balance, potentially augmenting the safety profile for bioelectrical applications (Supplementary Fig. 25c,d).

CMs photostimulation in vitro

We performed photostimulation on CMs cultured on glass-bottom dishes using monolithic Por-Si chips (Fig. 3a). In our 'insert-and-play' alternative to previous biointerfacing methods[29–33], the device is placed into the cell culture medium, in which it naturally lands and interacts with CMs. This method facilitates closer correlations between photocurrent measurements and biological-modulation scenarios, and avoids complications arising from photothermal or photoacoustic effects that may be substantial in tight biointerfaces[18,31,34].

We examined stimulation-induced Ca^{2+} influx and wave propagation using fluorescent calcium dye (Cal-520 AM). Optical pacing elicited synchronized calcium influx at 1 Hz with a 1-ms delivered pulse (Fig. 3b); no synchronization was achieved using an inert device or light only. We note that our previous work with Si nanowire-based CM interfaces yielded optical training effects but not overdrive pacing[35]. Adjusting the spot size from 200 µm to 10 µm, we successfully reduced the excited cellular area from hundreds of cells down to a single cell within the imaging frame time of 83 ms (Fig. 3c and Supplementary Videos 5–7). The initial area of excitation correlated strongly with the localized photostimulation, in which optically activated cells initiated intercellular Ca^{2+} propagation (Fig. 3d and Supplementary Fig. 26).

Near-field electrical stimulation, or point stimulation, leads to localized virtual electrodes based on the activation function theory, enabling precise cell activation control. This causes unique membrane depolarization patterns, such as the 'dog-bone' shape seen in highly oriented cardiac tissues[36–38]. Meanwhile, far-field stimulation produces a more uniform depolarization across the target tissue[39]. However, the phenomenon of photodepolarization of the cell membrane, especially its origin and dynamics, remains underexplored. CMs were loaded with membrane-voltage dyes (FluoVolt) for visualizing this process. Successful pacing at different frequencies were achieved (Supplementary Video 8). Following light stimulation, we observed localized photostimulation effect in the randomly oriented cell culture, inducing membrane-voltage distributions and propagation patterns distinct from those observed without stimulation (Fig. 3e, top versus bottom rows and Supplementary Fig. 27). Stimulations at sub-threshold or near-threshold optical intensities result in less evident depolarization and propagation (Supplementary Fig. 28).

The monolithic photoelectrochemical device can also be applied to intracellular Ca^{2+} dynamics and drug-related experiments. Measurements of amplitude, decay and time-to-peak (ToP) of the intracellular Ca^{2+} concentration ($[Ca^{2+}]i$) did not show substantial changes before and after pacing at around 1 Hz (Supplementary Fig. 29a,d). Following cell exposure to different concentrations of isoproterenol, a marked reduction in ToP was observed, suggesting a faster dynamic response (Supplementary Fig. 29b,e). Following exposure to high concentrations of nifedipine, a known L-type Ca^{2+} channel blocker, cells under pacing showed a notable decrease in intracellular Ca^{2+} amplitude during their systolic–diastolic cycles and experienced a longer decay time after activation, indicating sarcolemma-mediated Ca^{2+} influx (Supplementary Fig. 29c,f). We also demonstrated optical pacing of adult CMs at 1 Hz, 2 Hz and 3 Hz. The presence of T-tubules results in more effective electrical-contraction coupling and the ToP of adult rat CMs was substantially shortened compared with neonatal CMs (Supplementary Fig. 30). The effect of nifedipine on adult rat CMs Ca^{2+} dynamics is considerably less than that of the neonatal CMs (Supplementary Fig. 31), suggesting that a more developed cellular structure (that is, sarcoplasmic reticulum) in adult CMs could facilitate calcium handling[40].

Neonatal rat CMs are sensitive to Ca^{2+} changes during maturation. However, no marked changes in cell spreading area or myofibril morphology were observed at days 1, 2 and 5 post-stimulation (Supplementary Fig. 32) or in the expression of Fos, cTnT, Nrf1, Gja1 and Actc1 (reverse transcription quantitative polymerase chain reaction (RT-qPCR) at day 5) (Supplementary Fig. 33). Increased Gata4 levels when the Por-Si device is present might be because of non-electrical factors, such as the weight or degradation products of the device, as light was not a contributing factor. The absence of changes may be because of the short period or pacing parameters. However, the optical-pacing platform presents a promising tool for future cellular mechanistic studies and longer-term pacing studies in vitro with device passivation (Supplementary Figs. 34 and 35).

Photostimulation of rat heart ex vivo

We interfaced monolithic membranes composed of PIN-Si, PIN-Si (Au) and Por-Si with isolated rat hearts in a Langendorff setup. As illustrated

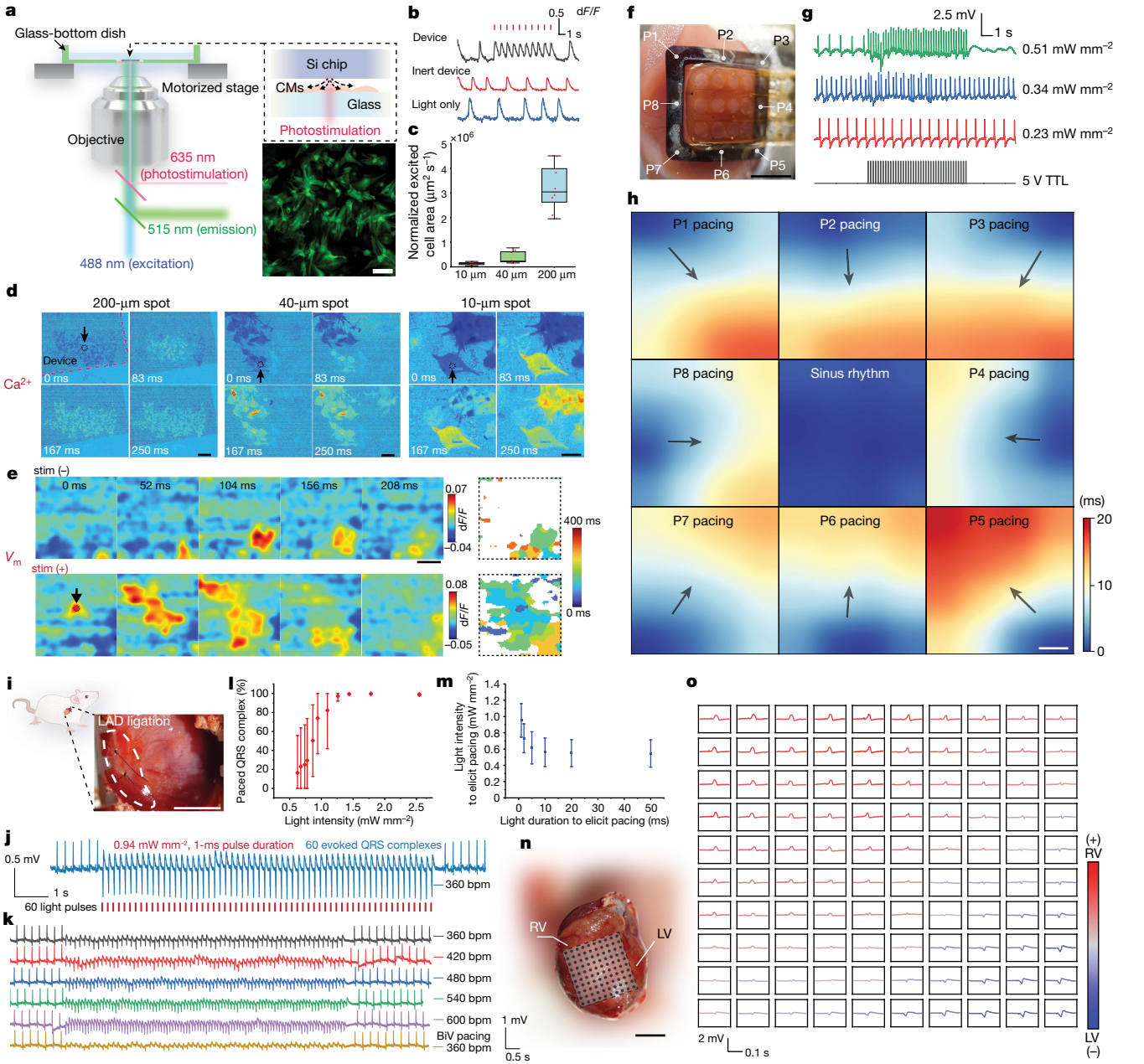

Fig. 3 | Spatiotemporal photostimulation in multiscale cardiac systems. **a**, Experimental setup of in vitro-cultured CMs photostimulation with fluorescent imaging. Inset shows representative CMs fluorescent image stained by Cal-520 AM from $N = 6$ different culture groups. Scale bar, 100 μm. **b**, dF/F plot shows neonatal rat CMs optical pacing at 1 Hz (4 mW, 1-ms pulse, 80-μm spot). Inert device: pristine p-type silicon. **c**, Plot of excited cell area after photostimulation at various spot sizes within one frame (83 ms). Boxes bind interquartile range (IQR) divided by median; whiskers extend 1.5 times the IQR. **d**, Spatiotemporal dF/F fluorescent images show calcium influx and propagation following stimulation with different spot sizes. Scale bars, 500 μm (200-μm spot), 100 μm (40-μm spot), 50 μm (10-μm spot). For **c** and **d**, $N = 8$ locations from $N = 4$ parallel cell culture groups. **e**, Imaging of membrane voltage (V_m) before and after light stimulation. Scale bar, 1 mm. **f**, Ex vivo rat heart setup for multisite stimulation and recording. Scale bar, 4 mm. **g**, Pacing of ex vivo rat heart at varying optical intensities illustrates full capture, partial capture and non-capture. **h**, Isochrone map shows electrical signal activation delay after photostimulation of eight different locations on open-window-structured monolithic Si device. Scale bar, 1.2 mm. For **f**–**h**, images and plots are representative of two biological replicates. **i**, Photograph of LAD ligation-induced ventricular ischaemia. Scale bar, 5 mm. **j**, Optical pacing of ischaemic rat heart model at 360 bpm. **k**, Optical pacing of ischaemic rat heart at different bpm, 1.26 mW mm^{-2}, pulse 1 ms. Biventricular (BiV) pacing at 360 bpm. For **i**–**k**, images and plots are representative of three biological replicates. **l**, Photostimulation success rate with 1-ms pulse duration. $N = 3$ rats, $N = 6$ devices. $N = 60$ QRS peaks evaluated for each device. **m**, Optical-power threshold for uninterrupted pacing of heart tissue at various light durations. $N = 3$ rats, $N = 6$ devices. For **l** and **m**, data are expressed as mean ± s.d. **n**, Illustration of high spatiotemporal multisite stimulation on rat heart. A blurred background was added to improve the image clarity and remove sensitive content. Scale bar, 5 mm. **o**, ECG traces illustrating pacing map of 100 distinct paced QRS waveforms. LV, left ventricle; RV, right ventricle. The upper and lower limits of the colour bar are determined by the maximum positive peak value associated with RV activation and the maximum negative peak value associated with LV activation, respectively.

by the recorded electrocardiogram (ECG), the PIN-Si membrane failed to synchronize the heartbeat frequencies with the delivered light pulse at 240 bpm, even at a light intensity of 177 mW mm^{-2} (Supplementary Fig. 36). The increased photoelectrochemical current of PIN-Si (Au) achieved pacing of the isolated heart at 240 bpm using an optical intensity of 141 mW mm^{-2}. With Por-Si, the minimal intensity required

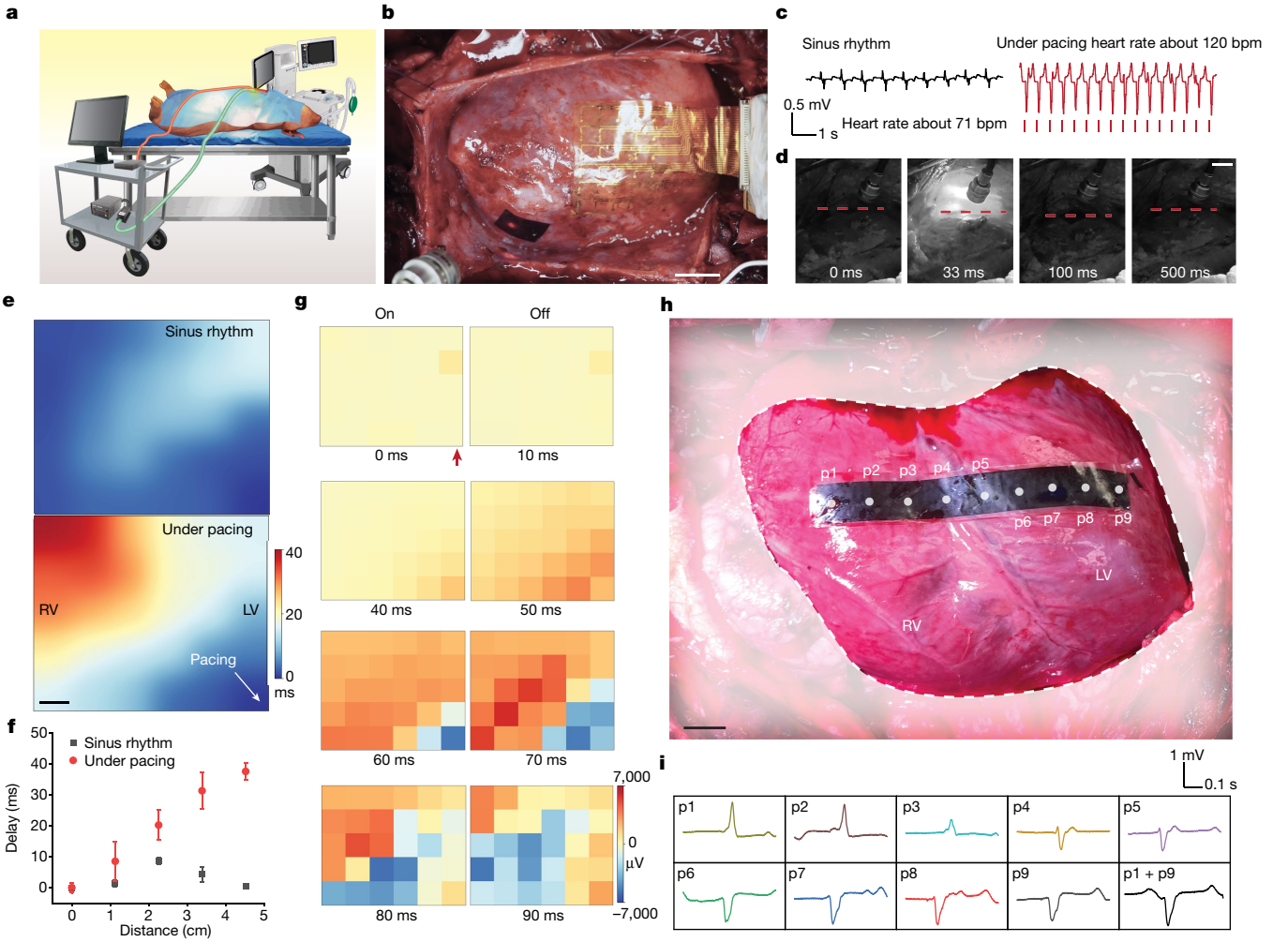

Fig. 4 | Translational photostimulation on a live pig heart. a, Schematic illustration of an adult pig in an open-thoracic cardiac-pacing experiment. The setup includes a health-monitoring station, an anaesthesia ventilation system, a workstation controlling the laser source and a recording hub connected to an epicardial flexible MEA. **b**, Photograph showing placement of a monolithic Si membrane conformally attached to the ventricular wall and a flexible MEA for recording electrical signals directly from the heart surface. Scale bar, 2 cm. **c**, Representative plots demonstrate overriding of the original heartbeat (71 bpm) to a designated frequency (120 bpm) and paced QRS complexes. The pacing capability was validated with experiments on $N = 3$ individual pigs. **d**, Snapshots of a ventricular-pacing event following photostimulation. The epicardial surface (dashed red line) moved down after laser stimulation, indicating systole caused by electrical stimulation, followed by diastole just before the next photostimulation. Scale bar, 2 cm. **e**, ECG isochrone shows the activation delay between left and right ventricular muscles. For each isochrone map, $N = 5$ ECG peaks were averaged from $N = 3$ independent recordings, $N_{peaks} = 15$. Scale bar, 6 mm. **f**, Plot of ECG signal delay diagonally along the MEA from the pacing location. $N = 2$ diagonal channels in the 30-channel MEA from $N = 3$ independent recordings were used for the plot, $N = 6$. Data are expressed as mean ± s.d. **g**, Time-resolved heat maps depicting peak intensity over time show electric-signal propagation originating from the pacing location (red arrow). Plots are representative of pacing trials from three devices. **h**, Device placement on the pig heart, designed for multisite optical pacing across both left and right ventricles. The device measures 0.96 cm × 7.96 cm, with each pacing point evenly spaced by approximately 0.9 cm. A blurred white background was added to enhance the clarity of the image and remove the sensitive content. Scale bar, 1 cm. **i**, Representative evoked ECG waveforms following multisite photostimulation. LV, left ventricle; RV, right ventricle. For **h**,**i**, the image and plots are representative of three pacing trials from one pig heart.

for stable pacing was reduced to 0.166 mW mm^{-2}. Stable pacing of the heart at 360 bpm was also observed (Supplementary Video 9). A systematic investigation of membrane designs and pacing conditions that affect the threshold optical intensity for pacing was performed (Supplementary Fig. 37).

For multisite pacing, the Por-Si device was further engineered to feature an open window, which accommodated a flexible, 16-channel multielectrode array (MEA) (Fig. 3f and Supplementary Fig. 38). Photostimulation was performed on the Por-Si frame with 240-bpm pacing frequency and 1-ms duration (Fig. 3g and Supplementary Fig. 39a). Under different applied intensities, capture, partial capture and non-capture of the override heart-pacing effects were observed. Before multisite pacing, we examined the photocurrent profile following backside illumination of the membrane to ensure consistency in resolution (Supplementary Fig. 40a,b). Spatially distinct photocurrent peaks, the result of two simultaneous light sources (Supplementary Fig. 40c), indicated potential for multisite or simultaneous stimulation. High spatiotemporal multisite pacing was performed by locally targeting the light spot on the eight different sites on the device with 1-ms optical pulses. At each pacing site, the recorded multiplexed electrical signals in the cardiac tissue showed varying time points of the QRS waveforms, indicating varying activation delays (Fig. 3h, Supplementary Video 10 and Supplementary Fig. 39b). This result indicates that the monolithic device can execute leadless high spatiotemporal

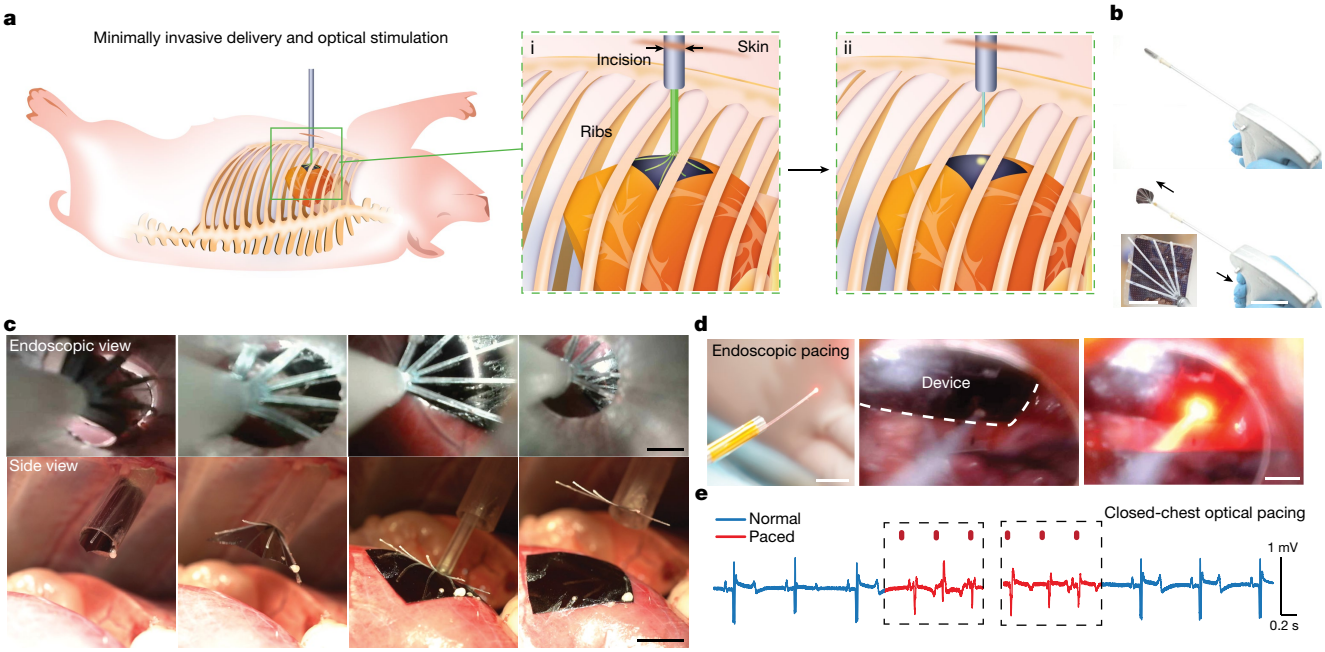

Fig. 5 | Minimally invasive approach for closed-thoracic modulation. **a**, Schematic representation depicting an incision through the intercostal space, followed by catheter-based delivery of the Si device (i) and subsequent optical-fibre photostimulation (ii). **b**, Photographs illustrating the flexible-membrane device housed in the custom delivery device (top) and unrolling and release of the device following trigger-pulling (bottom). Inset shows an enlarged view of the actual Si membrane device attached to the substrate. Scale bars, 4 cm (main), 1 cm (inset). **c**, Endoscopic and side-view photographs of the device-delivery process in a sheep cadaver for preliminary investigations before the actual pig heart in vivo experiment. Scale bars, 5 mm (endoscopic view), 1 cm (side view). **d**, Photographs of optical-fibre-coupled endoscope and endoscopic views during the minimally invasive pig heart pacing process. Scale bars, 1 cm (left), 5 mm (shared by middle and right). **e**, Paced ECG waveforms derived from a fully closed-thoracic procedure using 1-ms optical pulses. An uncollimated fibre optics was used for this proof-of-concept study, yielding optical intensities between 1 and 100 mW mm^{-2}. Plots are representative of seven pacing trials from one pig heart.

photostimulation, effectively controlling the activation initiation point on cardiac tissue by the light-spot location.

Rodent photostimulations in vivo

The in vivo heart-pacing experiment is more complex, as cardiac activity is influenced by the autonomic nervous system and involves inter-organ interactions[41]. To demonstrate reliable pacing in a compromised heart, we performed left anterior descending artery (LAD) ligation in a rat model to induce acute ischaemia (Fig. 3i). ECG traces suggested an increased heartbeat, potentially a compensatory response to ischaemia, as well as fluctuating baselines indicative of pronounced breathing patterns (Extended Data Fig. 5a). The Por-Si device reliably paced ischaemic in vivo cardiac tissue at 360 bpm with 1-ms light-pulse duration and optical intensities (0.94 mW mm^{-2}) comparatively lower than optogenetic approaches, in which an intensity of more than 1 mW mm^{-2} would generally be required[14] (Fig. 3j). Pacing reliability was demonstrated at elevated frequencies up to 600 bpm (Fig. 3k). With prolonged light-pulse durations, such as 10 ms, a lower threshold optical intensity (about 0.73 mW mm^{-2}) is necessary for consistent pacing (Fig. 3l and Extended Data Fig. 5b–d). We explored pacing durations from 1 ms to 50 ms, achieving a reduction in the threshold intensity necessary for pacing (Fig. 3m). Devices with different treatments were also investigated for the pacing-threshold studies (Supplementary Fig. 41).

Biventricular pacing is a clinically established CRT for ventricular dyssynchrony[42]. Two laser sources (635 nm and 473 nm) were used for simultaneous pacing of the left and right ventricles, using a single monolithic Por-Si device (Extended Data Fig. 5e). Biventricular photostimulation generated ECG waveforms in line with previous studies on rats using epicardial leads and clinically acquired data from patients with pacemakers[43,44] (Fig. 3k and Extended Data Fig. 5e). Concurrent activation of the left and right ventricles resulted in QRS durations not substantially different from the sinus rhythm, suggesting a route to optical CRT (ref. 42) (Extended Data Fig. 5f and Supplementary Fig. 42). Furthermore, consistent pacing at 360 bpm for more than 5 min was achieved at an optical intensity of 1.22 mW mm^{-2} (Extended Data Fig. 5g and Supplementary Fig. 43). High spatiotemporal photostimulation at 100 locations (Supplementary Fig. 44) on the monolithic device evoked varied QRS complexes, corresponding to a gradient change in the activation sequence between the left ventricle and the right ventricle (Fig. 3n,o). This finding suggests that monolithic Por-Si devices can facilitate high spatiotemporal multisite photostimulation on any exposed epicardial surface with millisecond deterministic light pulses, circumventing the constraints of predesigned microfabricated-device patterns.

To explore non-invasive transthoracic pacing, we implanted the Por-Si device in an in vivo mouse heart and closed the thorax. Pacing at 360 bpm was achieved with an intensity of 62.7 mW mm^{-2} and 10-ms pulse duration through the chest (Extended Data Fig. 6), a relatively lower power than that used in transthorax or transcranial optogenetics with irradiances greater than 100 mW mm^{-2} (refs. 13,45). No marked inflammation on mice was observed after a 7-day Por-Si film subcutaneous implantation (Supplementary Fig. 45).

Pig heart photostimulation in vivo

We applied our non-genetic optoelectronic technique to modulate cardiac activity in a live porcine model, with anatomical and functional resemblance to the human heart (Fig. 4a). Given the increase in heart size and potentially higher pacing threshold, we scaled up our device size to approximately 4 cm^2 for increased photocurrent (Supplementary Fig. 46). The Por-Si device was placed on the epicardial wall of

the right ventricle, conforming easily to the curvilinear ventricular wall without sutures or adhesives (Fig. 4b). Following optical pacing (approximately 23 mW mm^{-2}, 10-ms pulse), distinct ventricular-pacing waveforms were captured on clinical ECG grid paper (Extended Data Fig. 7a). Pacing with 2-Hz laser pulses resulted in an override heart rate of about 120 bpm, compared with resting of about 71 bpm (Fig. 4c). A snapshot shows a single optical-pacing event under 120 bpm (Fig. 4d and Supplementary Video 11). Movement of the heart surface was also tracked (Extended Data Fig. 7b). Deterministic pacing can be obtained by elevating the optical intensity, which mitigates any synchronization inconsistencies (Supplementary Video 12, 25.2 mW mm^{-2}, 40-ms pulse; Extended Data Fig. 7c, 25 mW mm^{-2}, 1-ms pulse). On the basis of three adult pigs weighing 50 kg, 83 kg and 100 kg, slight variations in pacing thresholds across different heart regions can be attributed to tissue heterogeneity and devices conformity. An optical intensity of 20–30 mW mm^{-2} with a 1-ms pulse duration can be firmly established as the threshold intensity for pig heart pacing using our device (4 cm^2 Por-Si membrane). The recorded ECG waveforms indicated that the sinus rhythm had a QRS duration of about 80 ms, corresponding to normal heart-conduction conditions. Following left-ventricular pacing, the QRS complex widened to approximately 140 ms owing to the time difference between left and right ventricular contraction events (Extended Data Fig. 7d).

A flexible, 30-channel MEA was positioned on the epicardium, covering a mapping area of 40 mm × 32 mm, to directly record epicardial electrical signals (Fig. 4b and Supplementary Figs. 47 and 48). The pacing device was placed on the left ventricle, anatomically bottom right relative to the MEA. The paced cardiac tissue overrode the original heart-conduction pathway, with propagation of electrical signal from the left ventricular surface to surrounding tissues (Fig. 4e and Supplementary Video 13). The propagation direction was also indicated by the ECG peak delay in the diagonal direction along the MEA (Fig. 4f), as well as in the longitudinal and transversal directions (Supplementary Fig. 49). Spatiotemporal mapping in Fig. 4g shows electrical-signal propagation on the epicardial surface.

During multisite pacing over different regions of the device (Fig. 4h, p1–p9), the recorded surface ECG waveforms reflect a gradient shift in muscle-activation sequences from the right to the left ventricle (Fig. 4i). Biventricular pacing can be exemplified by concurrently focusing two light beams on separate points on the left and right ventricles (Fig. 4i, p1 + p9). Comparable spatial control over cardiac activation in other regions of the heart surface are shown in Extended Data Fig. 7e,f.

Minimally invasive photostimulation

We devised a minimally invasive device-delivery technique for optical cardiac modulation, using a pig heart model to emulate clinical surgical procedures (Fig. 5a,b, Supplementary Methods, Supplementary Figs. 50 and 51 and Supplementary Video 14). Requiring only a small incision, 0.5–1 cm in diameter between two ribs (Fig. 5a,i), this approach avoids invasive cutting and spreading of ribs and associated post-operative trauma. Before device insertion, a microsurgical procedure exposes a diminutive window (1.5–2 cm) on the pericardium. The delivery-device catheter is introduced by means of the incision, enabling unrolling and secure placement of the Si membrane device on the epicardial surface (Fig. 5c). Once the delivery device is retracted, we introduce an optical-fibre-coupled endoscope through the incision, for visually guided optical stimulation (Fig. 5a,ii,d). Our trial proficiently executed the entire procedure in a closed-thoracic setting, resulting in the first minimally invasive optical stimulation of an in vivo pig heart (Fig. 5e). These findings reinforce the conceptual integrity of our approach, indicating translational potential for minimally invasive cardiac interventions in clinical settings. We believe that this demonstration of non-genetic optoelectronic heart pacing in a pig and the minimally invasive operation lays the groundwork for translational semiconductor-based photostimulation. Furthermore, the total weight of our pacemaker devices, including the polymeric substrates used to support the Si membranes, is 2–3 orders of magnitude lower than that of conventional pacemaker devices and, therefore, therapeutically advantageous to enhancing patient outcome.

Online content

Any methods, additional references, Nature Portfolio reporting summaries, source data, extended data, supplementary information, acknowledgements, peer review information; details of author contributions and competing interests; and statements of data and code availability are available at https://doi.org/10.1038/s41586-024-07016-9.

1. Kringelbach, M. L., Jenkinson, N., Owen, S. L. F. & Aziz, T. Z. Translational principles of deep brain stimulation. *Nat. Rev. Neurosci.* **8**, 623–635 (2007).
2. Krauss, J. K. et al. Technology of deep brain stimulation: current status and future directions. *Nat. Rev. Neurol.* **17**, 75–87 (2021).
3. Choi, Y. S. et al. Fully implantable and bioresorbable cardiac pacemakers without leads or batteries. *Nat. Biotechnol.* **39**, 1228–1238 (2021).
4. Gauvain, G. et al. Optogenetic therapy: high spatiotemporal resolution and pattern discrimination compatible with vision restoration in non-human primates. *Commun. Biol.* **4**, 125 (2021).
5. Fernandez-Ruiz, A., Oliva, A. & Chang, H. High-resolution optogenetics in space and time. *Trends Neurosci.* **45**, 854–864 (2022).
6. Entcheva, E. & Bub, G. All-optical control of cardiac excitation: combined high-resolution optogenetic actuation and optical mapping. *J. Physiol.* **594**, 2503–2510 (2016).
7. Jiang, Y. et al. Wireless, closed-loop, smart bandage with integrated sensors and stimulators for advanced wound care and accelerated healing. *Nat. Biotechnol.* **41**, 652–662 (2023).
8. Maya-Vetencourt, J. F. et al. A fully organic retinal prosthesis restores vision in a rat model of degenerative blindness. *Nat. Mater.* **16**, 681–689 (2017).
9. Ferlauto, L. et al. Design and validation of a foldable and photovoltaic wide-field epiretinal prosthesis. *Nat. Commun.* **9**, 992 (2018).
10. Mickle, A. D. et al. A wireless closed-loop system for optogenetic peripheral neuromodulation. *Nature* **565**, 361–365 (2019).
11. Yang, Y. et al. Wireless multilateral devices for optogenetic studies of individual and social behaviors. *Nat. Neurosci.* **24**, 1035–1045 (2021).
12. Hu, H. et al. A wearable cardiac ultrasound imager. *Nature* **613**, 667–675 (2023).
13. Hsueh, B. et al. Cardiogenic control of affective behavioural state. *Nature* **615**, 292–299 (2023).
14. Nussinovitch, U. & Gepstein, L. Optogenetics for in vivo cardiac pacing and resynchronization therapies. *Nat. Biotechnol.* **33**, 750–754 (2015).
15. Huang, Y. et al. Bioresorbable thin-film silicon diodes for the optoelectronic excitation and inhibition of neural activities. *Nat. Biomed. Eng.* **7**, 486–498 (2023).
16. Silverå Ejneby, M. et al. Chronic electrical stimulation of peripheral nerves via deep-red light transduced by an implanted organic photocapacitor. *Nat. Biomed. Eng.* **6**, 741–753 (2022).
17. Prominski, A. et al. Porosity-based heterojunctions enable leadless optoelectronic modulation of tissues. *Nat. Mater.* **21**, 647–655 (2022).
18. Jiang, Y. et al. Rational design of silicon structures for optically controlled multiscale biointerfaces. *Nat. Biomed. Eng.* **2**, 508–521 (2018).
19. Chenais, N. A. L., Airaghi Leccardi, M. J. I. & Ghezzi, D. Photovoltaic retinal prosthesis restores high-resolution responses to single-pixel stimulation in blind retinas. *Commun. Mater.* **2**, 28 (2021).
20. Mathieson, K. et al. Photovoltaic retinal prosthesis with high pixel density. *Nat. Photonics* **6**, 391–397 (2012).
21. Gaillet, V. et al. Spatially selective activation of the visual cortex via intraneural stimulation of the optic nerve. *Nat. Biomed. Eng.* **4**, 181–194 (2020).
22. Prévot, P. H. et al. Behavioural responses to a photovoltaic subretinal prosthesis implanted in non-human primates. *Nat. Biomed. Eng.* **4**, 172–180 (2020).
23. Buzsáki, G., Anastassiou, C. A. & Koch, C. The origin of extracellular fields and currents – EEG, ECoG, LFP and spikes. *Nat. Rev. Neurosci.* **13**, 407–420 (2012).
24. Mao, X. & Chen, P. Inter-facet junction effects on particulate photoelectrodes. *Nat. Mater.* **21**, 331–337 (2022).
25. Sambur, J. B. et al. Sub-particle reaction and photocurrent mapping to optimize catalyst-modified photoanodes. *Nature* **530**, 77–80 (2016).
26. Lei, Y. et al. A fabrication process for flexible single-crystal perovskite devices. *Nature* **583**, 790–795 (2020).
27. Lei, Y. et al. Perovskite superlattices with efficient carrier dynamics. *Nature* **608**, 317–323 (2022).
28. Qian, Q. et al. Photocarrier-induced persistent structural polarization in soft-lattice lead halide perovskites. *Nat. Nanotechnol.* **18**, 357–364 (2023).
29. Fang, Y. et al. Micelle-enabled self-assembly of porous and monolithic carbon membranes for bioelectronic interfaces. *Nat. Nanotechnol.* **16**, 206–213 (2021).
30. Parameswaran, R. et al. Photoelectrochemical modulation of neuronal activity with free-standing coaxial silicon nanowires. *Nat. Nanotechnol.* **13**, 260–266 (2018).
31. Jiang, Y. et al. Heterogeneous silicon mesostructures for lipid-supported bioelectric interfaces. *Nat. Mater.* **15**, 1023–1030 (2016).
32. Rotenberg, M. Y. et al. Living myofibroblast–silicon composites for probing electrical coupling in cardiac systems. *Proc. Natl Acad. Sci.* **116**, 22531–22539 (2019).

33. Rotenberg, M. Y. et al. Silicon nanowires for intracellular optical interrogation with subcellular resolution. *Nano Lett.* **20**, 1226–1232 (2020).
34. Maya-Vetencourt, J. F. et al. Subretinally injected semiconducting polymer nanoparticles rescue vision in a rat model of retinal dystrophy. *Nat. Nanotechnol.* **15**, 698–708 (2020).
35. Parameswaran, R. et al. Optical stimulation of cardiac cells with a polymer-supported silicon nanowire matrix. *Proc. Natl Acad. Sci.* **116**, 413–421 (2019).
36. Nikolski, V. P., Sambelashvili, A. T. & Efimov, I. R. Mechanisms of make and break excitation revisited: paradoxical break excitation during diastolic stimulation. *Am. J. Physiol. Heart Circ. Physiol.* **282**, H565–H575 (2002).
37. Sobie, E. A., Susil, R. C. & Tung, L. A generalized activating function for predicting virtual electrodes in cardiac tissue. *Biophys. J.* **73**, 1410–1423 (1997).
38. Wikswo, J. P., Lin, S. F. & Abbas, R. A. Virtual electrodes in cardiac tissue: a common mechanism for anodal and cathodal stimulation. *Biophys. J.* **69**, 2195–2210 (1995).
39. Gillis, A. M., Fast, V. G., Rohr, S. & Kléber, A. G. Spatial changes in transmembrane potential during extracellular electrical shocks in cultured monolayers of neonatal rat ventricular myocytes. *Circ. Res.* **79**, 676–690 (1996).
40. Louch, W. E., Koivumäki, J. T. & Tavi, P. Calcium signalling in developing cardiomyocytes: implications for model systems and disease. *J. Physiol.* **593**, 1047–1063 (2015).
41. Herring, N., Kalla, M. & Paterson, D. J. The autonomic nervous system and cardiac arrhythmias: current concepts and emerging therapies. *Nat. Rev. Cardiol.* **16**, 707–726 (2019).
42. Vernooy, K., van Deursen, C. J. M., Strik, M. & Prinzen, F. W. Strategies to improve cardiac resynchronization therapy. *Nat. Rev. Cardiol.* **11**, 481–493 (2014).
43. Haeberlin, A. et al. Conduction system pacing today and tomorrow. *J. Clin. Med.* **11**, 7258 (2022).
44. Mulla, W. et al. Prominent differences in left ventricular performance and myocardial properties between right ventricular and left ventricular-based pacing modes in rats. *Sci. Rep.* **7**, 5931 (2017).
45. Chen, R. et al. Deep brain optogenetics without intracranial surgery. *Nat. Biotechnol.* **39**, 161–164 (2021).

Methods

Further methods can be found in the supporting information.

Fabrication of silicon-chip devices

sPN-Si. sPN-Si (orientation (111), n-type layer, 44.5 ± 1 μm, 1.1 ohm cm; p-type layer, 381 μm, 0.004–0.008 ohm cm) was obtained from Nova Electronic Materials and diced using a Disco DAD3240 dicing saw for direct characterizations.

PIN-Si. PIN-Si was prepared using the chemical vapour deposition method. A p-type Si wafer or a silicon-on-insulator (SOI) wafer was used as the substrate for deposition of intrinsic and n-type layers. Before deposition, the substrate was cut into dimensions 4 cm × 2 cm and cleaned in an ultrasonic bath for 3 min in acetone and 3 min in isopropyl alcohol (IPA), and then rinsed with deionized (DI) water. The wafer was soaked in 10% hydrofluoric acid (HF) for 5 min to remove the native oxide and then placed inside a quartz tube for evacuation. The i-type and n-type layers were deposited under 650 °C with 15 torr chamber pressure for 20 min. Flow rates of H_2 and SiH_4 were set as 60 and 0.3 sccm for the i-layer, respectively. The same settings were used for the n-layer with an extra 1.5 sccm flow rate for the dopant gas, PH_3 (1,000 ppm in H_2).

PIN-Si (Au). The PIN-Si chip was decorated with gold nanoparticles using electroless deposition. The PIN-Si chip was first dipped in 10% HF for 3 min to remove any potential oxide layer. It was then dipped in an electroless deposition solution consisting of 1% HF and 1 mM $HAuCl_4$ for 2 min.

Por-Si. We present three techniques for creating nanoscale pores in p-type Si (orientation (100), resistivity 0.001–0.005 ohm cm, Nova Electronic Materials), including metal-assisted chemical etching (MACE), stain-etching and a combination of both methods. Before etching, the wafers were diced using a Disco DAD3240 dicing saw and subsequently cleaned in an ultrasonic bath for 3 min in acetone and 3 min in IPA. For MACE, Si chips were first dipped in 10% HF for 3 min. They were then immersed in an electroless deposition solution containing 1% HF and 1 mM silver nitrate ($AgNO_3$) for 2 min, and rinsed with DI water. The silver-decorated Si chips were then submerged in an etching solution consisting of 50% HF and 30% hydrogen peroxide (H_2O_2) at a 20:1 volume ratio for 3 min. Afterward, the Si chips were soaked in concentrated nitric acid (HNO_3) for 2 min to remove the silver. For stain-etching, the process was slightly modified from previously reported procedures to improve photocurrents[17]. The Si chips were immersed in a mixture of HF and HNO_3 at a volume ratio of 100:1 for 1 min, followed by soaking in concentrated HNO_3 for 1 min to oxidize and activate the surface. For the combined stain-MACE process, the Si chips were submerged in a solution of HF and HNO_3 with a 100:1 volume ratio, as well as 1 mM $AgNO_3$, for 3 min. The chips were then soaked in concentrated HNO_3 for 2 min to remove the silver. The as-prepared Por-Si samples were exposed to 400 W oxygen plasma at a flow rate of 50 sccm for 10 min in a Plasma-Therm inductively coupled plasma fluoride etcher, without radiofrequency bias.

Fabrication of monolithic Si membrane

SOI wafers (p++; device, 7 ± 1 μm, <0.005 ohm cm; handle, 300 ± 10 μm, 1–30 ohm cm; buried oxide, 1 μm) were sourced from Ultrasil. The photomask was designed using AutoCAD software and can be found in Supplementary Fig. 52. The fabrication process adhered to standard lithography techniques. A thick positive resist AZ40XT-11D (MicroChemicals) served as a mask for reactive ion etching. Patterns were exposed using the Heidelberg MLA150 direct writer, and the uncovered SOI was removed using an SF_6/CHF_3 (20 sccm:50 sccm) reactive ion etching process (inductively coupled plasma, 600 W; radiofrequency, 60 W) in a Plasma-Therm inductively coupled plasma fluoride etcher, with an etching rate of about 660 nm min^{-1}. The photoresist was stripped using AZ NMP (MicroChemicals) and the wafers were cleaned in an ultrasonic bath for 3 min in acetone, followed by 3 min in IPA and dried using compressed nitrogen. Samples were immersed in concentrated buffered HF (Thermal Scientific) overnight (roughly 12 h) to eliminate buried oxide layers. Membranes, along with the handle wafer, were subsequently rinsed twice for 1 min each in separate DI water baths to remove any residual HF. Wafers were then soaked in an IPA bath for 1 min and transferred to an acetone bath to facilitate interactions between the membranes and handle wafer. Last, free-floating membranes were moved to a fresh IPA bath using filter paper and stored at 4 °C before undergoing further processing. An optional supporting substrate for Si membranes, to facilitate device handling, was made of polydimethylsiloxane (10:1, Sylgard 184) coated polyethylene terephthalate (Sigma-Aldrich) with thicknesses of approximately 5 μm and 12.5 μm, respectively.

Standard photocurrent measurements

Photocurrent measurements were generally conducted in accordance with previously established methods[18]. A custom-made patch-clamp setup, integrated with an upright microscope (Olympus, BX61WI) featuring ×20/0.5 and ×40/0.5 numerical aperture water-immersion objectives, was used to measure photocurrents. Light pulses were introduced through episcopic illumination, using a dichroic mirror (for 625-nm LED, FF660-Di02-25x36, Semrock) or Thorlabs protected silver mirrors (for 635-nm laser, PF10-03-P01, PFR10-P01). Clamp voltage and current were recorded using silver chloride electrodes and amplified by an AxoPatch 200B amplifier (Molecular Devices). Voltage-clamp levels and light pulsing were digitally regulated using transistor–transistor logic or analogue signals sent from a Digidata 1550 digitizer (Molecular Devices), controlled with Clampex software (Molecular Devices). Glass pipettes were created using a P-97 Micropipette Puller (Sutter Instrument), typically featuring a resistance of 1–4 MΩ and filled with 1× phosphate-buffered saline (PBS). For a standard measurement, the material was positioned at the centre of the field of view in a Petri dish filled with 1× PBS. The pipette tip was brought close to the material surface (<10 μm) and the measurement sequence was initiated. The sequence lasted 400 ms, with an initial voltage level of −0.5 mV between 100 and 300 ms. At 200 ms, a 10-ms light pulse was administered to provoke a photoresponse from the material. The holding current was adjusted so that the current at the first voltage level was near 0 pA (typically below 2,000 pA).

Photocurrent precision measurements

The precision of four distinct Si devices was evaluated by measuring nine individual points on 5 mm × 5 mm chips (Supplementary Fig. 9a). Points 1, 3, 7 and 9 were located at the corners; points 2, 4, 6 and 8 were situated at the edges; and point 5 was at the device centre. Precision maps were generated by averaging the results from four independent samples for each Si device. The s.d. was computed using the population s.d. derived from the nine measured points. A 625-nm collimated LED with 20-mW power provided the illumination, and the spot size measured about 750 μm.

Photocurrent spatiotemporal mapping

In this study, photocurrent mapping with illumination at the device centre (Fig. 2d and Supplementary Fig. 9b, right), edge (Extended Data Fig. 2a and Supplementary Fig. 9b, centre) and corner (Extended Data Fig. 2b and Supplementary Fig. 9b, left) is presented. Each map was constructed using 81 measurements, with each point separated by 0.5 mm in a 9 × 9 array on the 5 mm × 5 mm chip (Supplementary Fig. 9). For the centre-illumination photocurrent measurement, light was illuminated at point 41 for a total of 81 times. For each illumination, the photocurrent was recorded at one individual point by controlling the

micropipette location. This process was similarly performed for edge illumination (point 37) and corner illumination (point 73).

In the static heat maps presented in Fig. 2d and Extended Data Figs. 2 and 4a, the peak photocurrent values (which can be either positive or negative during illumination) at each measurement location are shown. The colour scale was normalized to the maximum photocurrent value recorded from the entire substrate during illumination. In the dynamic photocurrent map (Extended Data Fig. 4b and Supplementary Fig. 23), the colour of each individual pixel at certain time points is normalized to their respective (that is, from the same location) maximum and minimum values during the 20-ms recording (10 ms light on and 10 ms light off), better illustrating the polarity distribution and switch. A 625-nm collimated LED with 20-mW power was used for illumination, and the spot size measured about 750 µm.

The error value presented in photocurrent accuracy measurement was calculated by:

$$\mathrm{Err} = \frac{\sqrt{(p_{\mathrm{max,x}} - p_{\mathrm{il,x}})^2 + (p_{\mathrm{max,y}} - p_{\mathrm{il,y}})^2}}{\sqrt{(p_{\mathrm{centre,x}} - p_{\mathrm{il,x}})^2 + (p_{\mathrm{centre,y}} - p_{\mathrm{il,y}})^2}} \times 100\%$$

in which $p_{\mathrm{max,x}}$ and $p_{\mathrm{max,y}}$ are the coordinates of the location with maximum photocurrent, $p_{\mathrm{il,x}}$ and $p_{\mathrm{il,y}}$ are the coordinates of the illumination point, and $p_{\mathrm{centre,x}}$ and $p_{\mathrm{centre,y}}$ are the coordinates at the substrate centre.

Photocurrent localization profiling

Resolution profiling (Fig. 2e, Extended Data Fig. 3 and Supplementary Fig. 9c) was used to illustrate the photocurrent localization capability of the four Si devices. A 750-µm light spot was generated using a ×20/0.5 numerical aperture water-immersion objective in conjunction with a 625-nm collimated LED. A 120-µm light spot was produced using the same objective but using a 635-nm laser (Laserglow). By adjusting the lens position with a ×40/0.5 objective, a 35-µm light spot was obtained. The optical-power levels for the 750-µm, 120-µm and 35-µm spots were 20 mW, 20.5 mW and 16.5 mW, respectively.

The light spot was centred on the device and a micropipette was used to record the current localization profile, starting at a distance of 2 mm from the device centre on one side and finishing at 2 mm from the other side, covering a total span of 4 mm across the device centre. For Por-Si illuminated with 120-µm and 35-µm spots, a step size of 0.025 mm was used, whereas a step size of 0.05 mm was used for the others. The photocurrent FWHM was calculated by summing the distances at which the photocurrent reached half of its maximum value.

Measurements from two spots (Supplementary Fig. 9d) were facilitated by pairing a 635-nm laser (Laserglow) with a 1 × 2 multimode fibre-optic coupler (Thorlabs, TH400R5F1B). The two terminations of the fibre optics were connected to a mating sleeve (Thorlabs, ADAFC2), followed by a ferrule patch cable (Thorlabs, M81L01), quick-release interconnects (Thorlabs, ADAF2), and, finally, to the fibre-optic cannula (Thorlabs, CFMC22L20). Positioned from the rear of the sample, the two fibre-optic cannulas created 1-mm light spots by adjusting the distances. These light spots were set at intervals of 1.8 mm, 4.5 mm and 6.6 mm, allowing for the assessment of the linear photocurrent profile using a patch-clamp micropipette.

CMs Ca^{2+} imaging and intracellular Ca^{2+} transient studies under pacing

Nikon inverted microscope Ti2-E and NIS-Elements software were used to image and record the in vitro experiments. For the purpose of imaging CM calcium (Ca^{2+}) activity, we stained the cultured CMs using a concentration of 5 µM Cal-520 AM (AAT Bioquest), allowing them to incubate for 45 min at 37 °C. Following this, the culture media was discarded and washed twice using PBS. This was subsequently replaced with the living-cell imaging solution (LCIS, 140 mM NaCl, 2.5 mM KCl, 1.8 mM $CaCl_2$, 1 mM $MgCl_2$, 20 mM HEPES, pH = 7.4) with 20 mM glucose for imaging using Nikon inverted microscope Ti-2E. The imaging used an excitation wavelength of 488 nm and the emission peak for the dye is 515 nm. The 635-nm laser (Laserglow) with FC/PC multimodal optical fibre was coupled to the Nikon microscope and focused through the objectives. The laser spot size with good focus for 4×, 10×, 20× and 60× objectives should be 200 µm, 80 µm, 40 µm and 10 µm, respectively. A customized Arduino Nano board was used to trigger and control the laser pulse with resolution to 1 ms. To mitigate the laser artefacts during optical pacing, an emission filter (Chroma, ET535/70m) was used to allow lights only with wavelengths between about 500 nm to 568 nm to pass through.

Before loading Si devices, it will be washed in DI water followed by soaking in LCIS for 1 min. After that, the devices were placed upside down, with active sides interfacing the cells. It is critical to ensure that no bubbles are present between devices and cells, which could cause failure to pacing. Also, it is important not to press the device against cells to avoid cell damage.

For nifedipine and isoproterenol administered cell groups, cells will be loaded with drugs and incubated at 37 °C for 5 min before conducting the optical stimulation and imaging.

To quantitatively analyse intracellular calcium dynamics and concentrations, we adopted the pseudocalibration method as delineated by Trafford et al.[46]. This method uses the following equation to ascertain intracellular calcium concentration ($[Ca^{2+}]i$):

$$[Ca^{2+}]i = K_d(F - F_{\mathrm{min}})/(F_{\mathrm{max}} - F)$$

in which F is the fluorescence signal, F_{min} is the fluorescence in the absence of Ca^{2+}, F_{max} is the fluorescence in the presence of saturating Ca^{2+} and K_d is the dissociation constant of Cal-520 AM, which is 320 nM at 37 °C. In our analysis, given the high signal-to-noise ratio of the dye, F_{min} is assumed to be 0, a presumption that aligns with practices for dyes such as Fluo-3. F_{max} is determined by treating cells with 10 mM ionomycin in 100 mM Ca^{2+}. It is crucial to ensure that, during this process, the detection pixel value remains non-saturated. The amplitude is determined by the difference of Ca^{2+} concentration (nM) or fluorescent intensity (dF/F) between the diastole and systole. The ToP is measured by the time span between the onset of fluorescent intensity and peak intensity. The decay is calculated by the time span between the peak intensity and the point at which it decreases to 37% of its amplitude.

CMs membrane voltage (V_m) imaging

The FluoVolt Membrane Potential Kit (Thermo Fisher Scientific) was used for staining CMs membrane voltage according to the manufacturer's protocol. Cells were stained in LCIS with 20 mM glucose for 30 min at 37 °C. An excitation source of 488 nm and an emission filter of 500–568 nm were used for imaging. All of the spatiotemporal imaging was conducted through 4× objectives to cover a wide field of view (approximately 3.4 mm × 3.4 mm), with a stimulation light-spot size of about 200 µm.

Ex vivo multisite stimulation in an isolated heart

The isolated heart preparation followed previously described methods[17]. Briefly, adult male rats (400–500 g body weight) were heparinized and anaesthetized using open-drop exposure to isoflurane in a bell jar setup. The heart was excised and immersed in ice-cold HBSS buffer before cannulating the aorta in preparation for a Langendorff setup. An oxygenated HEPES-buffered Tyrode's solution was perfused through the cannulated aorta after passing through a heating coil and bubble trap (Radnoti). The heart was positioned in a water-jacketed beaker (Fisher Scientific). The system temperature was kept constant at 37 °C and the perfusion pressure was kept at 80–100 mmHg. To facilitate the left ventricular pressure balloon measurement when required, the left atrial appendage was gently removed. Perfusion and left ventricular

pressure were monitored using a BP-100 probe (iWorx) connected to the perfusion line and a water-filled balloon (Radnoti) inserted into the left ventricle, respectively. For ECG recordings, needle electrodes were positioned on the left ventricular wall and aorta, grounded on the cannula and connected to a C-ISO-256 preamplifier (iWorx). All signals (perfusion, left ventricular pressure and ECG) were amplified (400×) using an IA-400D amplifier (iWorx) and interfaced with a computer using a Digidata 1550 digitizer with Clampex software (Molecular Devices). For proof-of-concept pacing tests (Fig. 3g and Supplementary Fig. 36), the monolithic Si membrane was placed on the left ventricular wall and adhered to the heart with capillary force. Stimulation and recording were controlled using the Digidata 1550 digitizer. TTL pulse train signals of 5 V were used to trigger the laser pulses. For multisite photostimulation, the open-windowed Si membrane (Supplementary Fig. 39a) was placed on the epicardial surface spanning left and right ventricles. A 635-nm laser with approximately 1 mW mm^{-2} optical intensity and 4 Hz frequency was used. A 1-ms pulse was used to better decouple the photocurrent artefacts and ECG signals from the recording. The laser spot was directed to the eight different points sequentially, ensuring a stable pacing >5 s for each point. The flexible, 16-channel MEA was placed in the window to perform multichannel recording and mapping. The MEA was connected to a zero-insertion-force connector linked to an Intan Technologies RHD2132 chip headstage through an 18-pin electrode adapter board. Signals were recorded at 20 kS s^{-1} in the 50–1,000-Hz bandwidth. Videos were taken by a Sony α6100 camera with a 30-mm macro lens (E 3.5/30, Sony).

In vivo rat heart stimulation with LAD ligation

Adult rats (10–24 weeks, males and females, 400–500 g) were deeply anaesthetized with isoflurane (2–4%). The tongue was gently pulled sideways and forceps were used to insert a tracheal cannula connected with a ventilation system (Harvard Small Animal Ventilator Model 683). The parameters of ventilation were set by following ref. 47. The fur was removed from the chest, right and left clavicle and left hip using surgical clippers and hair-removal cream. The ECG electrodes were placed on the left clavicle, right clavicle and left hip. The costal cartilages were cut along the left side of the sternum between the third and fifth intercostal ribs to expose the left ventricle. The pericardium was gently cleared away from the surface using forceps and cotton swabs. A small-animal rib spreader was used to open the thoracic space. A surgical needle with suture wire (8/0) was used to ligate the LAD to induce ischaemia; the ventricular wall became pale in appearance immediately after ligation. The Si membrane was then attached to the epicardial surface.

Multisite (100-point) rat heart stimulation was performed with the assistance of a manual linear stage (World Precision Instruments, KITE-R), enabling a 10 × 10 uniformly spaced stimulation array within a 1-cm^2 device area (Supplementary Fig. 44). The ECG waveforms are colour-coded on the basis of peak values to highlight the gradient change in spatial muscle activation (Fig. 3l,m). An Intan Technologies RHD2216 chip headstage (16 bipolar channels) with commercial sticky-pad electrode were used to record surface ECG signals in the Lead II position. Signals were collected at a sampling rate of 2 kS s^{-1} within a frequency bandwidth of 0.6–100 Hz.

In vivo pig heart stimulation

An adult female pig was deeply anaesthetized using inhalant anaesthesia administered by means of a vaporizer connected to a ventilator. The vital signs of the animal, including ECG, heart rate, end-tidal CO_2, blood oxygen saturation (SPO_2), respiratory rate, blood pressure and temperature, were continuously monitored at a monitoring station. The pig was positioned in the supine position and a median sternotomy was performed to expose the heart. After opening the pericardium, the Si membrane device was placed on the right ventricular wall of the cardiac tissue. Epicardial recordings were obtained by interfacing the cardiac tissues with a MEA positioned mostly on the upper part of the right ventricle. The MEA was connected to a zero-insertion-force connector, which was then linked to an Intan Technologies RHD2132 chip headstage (32 channels) through a 36-pin electrode adapter board. Signal recordings were collected at a sampling rate of 20 kS s^{-1} within a frequency bandwidth of 0.1–2,000 Hz. In multisite pig heart stimulation, a device size of 1 cm × 8 cm was used to cover a larger area of the heart. Stimulation was performed by pointing the laser at various points, as denoted in Fig. 4h and Extended Data Fig. 7e–g. An Intan Technologies RHD2216 chip headstage (16 bipolar channels) with commercial sticky-pad electrode were used to record surface ECG signals in the Lead II position. Signals were collected at a sampling rate of 2 kS s^{-1} within a frequency bandwidth of 0.6–100 Hz.

Closed-thoracic in vivo pig heart stimulation

We first used a sheep cadaver model to validate the feasibility of the device-delivery protocol, as shown in Fig. 5c. The device was smoothly deployed on the non-beating sheep heart. In the in vivo pig heart experiment, an adult female pig was thoroughly anaesthetized and prepped in a manner consistent with the open-thoracic in vivo pacing procedure. An incision was made between the third and fourth or the fourth and fifth intercostal spaces using a surgical electroceutical pen to access the heart ventricle. Using surgical scissors, a small window (1.5–2 cm) was created in the pericardium. An endoscope could be introduced to assist with the procedure. The delivery device was then inserted through the incision until the beat of the ventricle was felt. This was followed by the injection of the rolled Si membrane, ensuring that it formed a conformal contact with the ventricle. The natural fluid on the heart surface provided adequate moisture for device release. Alternatively, saline solution could be introduced by means of the tube to aid in adhesive dissolution. Once the Si membrane device was attached to the heart ventricle, the delivery device was removed. A 0.5-mm commercial poly(methyl methacrylate) fibre-optics-coupled endoscope (Oiiwak) was then introduced for visually guided photostimulation. The surface ECG recorded with commercial adhesive electrode pad through Intan Technologies RHD2216 chip headstage. Signal recordings were collected at a sampling rate of 2 kS s^{-1} within a frequency bandwidth of 0.6–100 Hz.

Data processing and statistics

We analysed data with Python scripts using the NumPy, Matplotlib, tifffile, SciPy, statsmodels and pandas libraries. Plotting was performed with Origin and Python Matplotlib. Statistics were calculated using the scipy.stats library, as well as the statsmodels library, unless otherwise clarified. For s.d. calculations, population s.d. was used for Fig. 2c, whereas others used sample s.d. Images were processed using ImageJ software. The fluorescence dF/F videos and images were processed using ImageJ and customized Python code with the tifffile library. An 8 × 8 binning and smoothing (sigma = 2) was applied to map spatiotemporal CMs membrane potential distributions. Customized Python code is used to generate isochrones. Codes are available in the online repository. Tracking of pig heart surface movement used the ImageJ Manual Tracking plug-in. The recordings from the 16-channel MEA on the ex vivo rat heart and the 30-channel MEA on the in vivo pig heart were analysed by customized Python scripts. Gaussian interpolation was used to enhance readability for presenting heat maps. Adobe Premiere Pro was used for video editing.

Reporting summary

Further information on research design is available in the Nature Portfolio Reporting Summary linked to this article.

Data availability

The research findings presented in this study are substantiated by the data included in the main body of the article, as well as its

Supplementary information. The source data and raw data are made readily accessible at https://osf.io/kr67g/. mRNA accession numbers: Actc1: NM_019183(1); Gata4: NM_144730(1); Nrf1: NM_001100708(1); Fos: NM_022197(1); Gapdh: NM_017008(1); Gja1: NM_012567(1); cTnT: NM_012676.2. Source data are provided with this paper.

Code availability

Scripts used for data analysis in this study can be accessed from https://osf.io/kr67g/.

46. Trafford, A. W., Díaz, M. E. & Eisner, D. A. A novel, rapid and reversible method to measure Ca buffering and time-course of total sarcoplasmic reticulum Ca content in cardiac ventricular myocytes. *Pflüg. Arch.* **437**, 501–503 (1999).
47. Kleinman, L. I. & Radford, E. P. Ventilation standards for small mammals. *J. Appl. Physiol.* **19**, 360–362 (1964).

Acknowledgements We thank K. M. Watters for scientific editing of the manuscript. This work was supported by the National Institutes of Health (1R56EB034289-01), the U.S. Air Force Office of Scientific Research (FA9550-20-1-0387), the National Science Foundation (NSF CBET-2128140, NSF DMR-2105321 and NSF MPS-2121044) and the U.S. Army Research Office (W911NF-21-1-0090). We would like to thank the University of Chicago Animal Resources Center (RRID: SCR_021806), especially the Carlson Large Animal clinic staff, A. Ostdiek, D. Mailhiot, J. McGrath, A. Brown, E. Becerra and P. Latalladi, for their assistance with the animal surgery. This work made use of the Pritzker Nanofabrication Facility at the Pritzker School of Molecular Engineering at the University of Chicago, which receives support from the Soft and Hybrid Nanotechnology Experimental (SHyNE) Resource (NSF ECCS-2025633), a node of the National Science Foundation's National Nanotechnology Coordinated Infrastructure (RRID: SCR_022955). We thank C. He for providing us the use of RT-qPCR systems. We thank F. Shi, Y. Jiang and A. Prominski for the help on the STEM imaging; this work made use of instruments in the Electron Microscopy Service (Research Resources Center, University of Illinois Chicago).

Author contributions B.T. and N.H. supervised the research. P.L. and B.T. initiated and conceived the Si-based photostimulation device concept. P.L. conducted most of the data collection on materials synthesis, characterization and animal experiments. P.L. designed and fabricated all the devices. J.Z. assisted with in vitro and ex vivo experiments. H.H. assisted with in vivo pig experiments. J.Y. assisted with in vitro and in vivo rodent experiments. W.L., C.Y., C.S. and J.S. assisted with materials preparation and characterization. J.H.-S. assisted with in vitro experiments. P.L. conducted all the subsequent data analysis. P.L. and B.T. prepared the manuscript, with input from all other authors.

Competing interests The University of Chicago filed provisional patent applications for the Si-based photostimulation platform and applications in multisite and minimally invasive cardiac modulation. B. Tian, P. Li, N. Hibino and H. Hayashi are the inventors. All remaining authors declare no competing interests.

Additional information
Supplementary information The online version contains supplementary material available at https://doi.org/10.1038/s41586-024-07016-9.

Correspondence and requests for materials should be addressed to Narutoshi Hibino or Bozhi Tian.

Peer review information *Nature* thanks Igor Efimov, Francesco Lodola and the other, anonymous, reviewer(s) for their contribution to the peer review of this work. Peer reviewer reports are available.

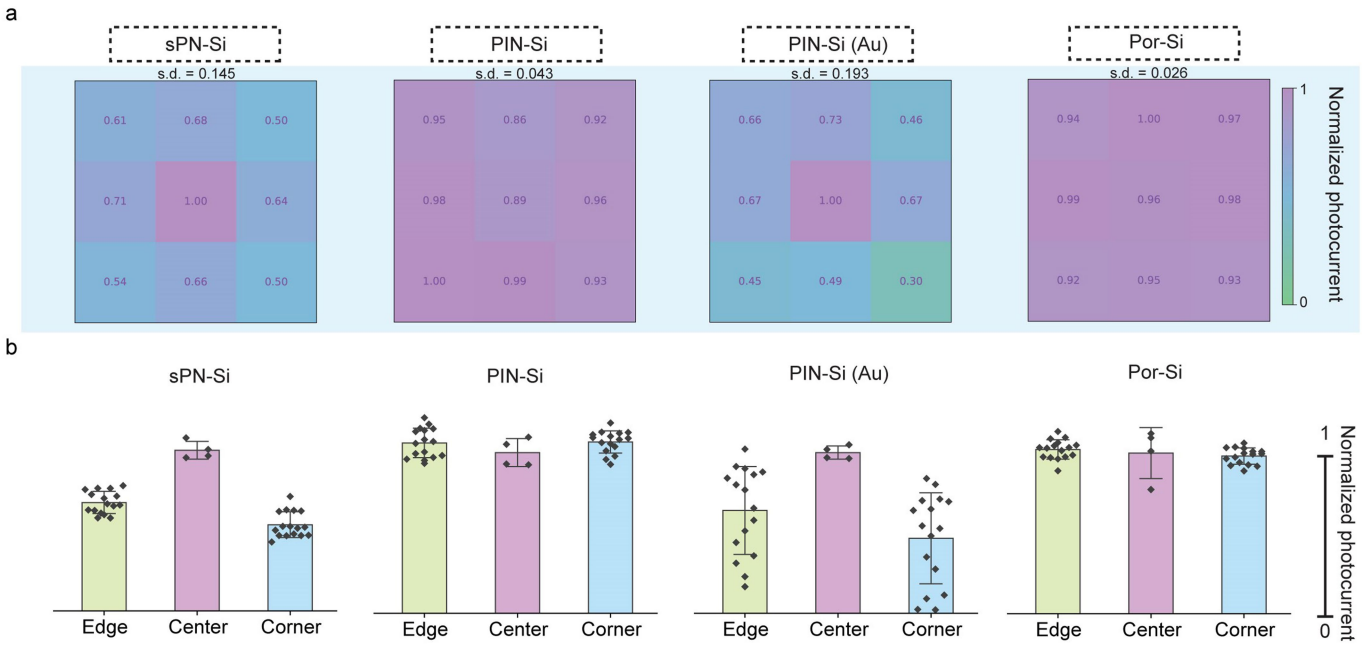

Extended Data Fig. 1 | Characterization of photocurrent precision for the four Si-based devices. The measurement includes nine-point photocurrent measurements at the centre, edge and corner of each device. Smaller variance in the nine-point results indicates more precise random-access photostimulation across different device locations. **a**, Three-by-three map showing the distribution of normalized averaged photocurrent peak value on each of the nine points. s.d. is calculated from the $N = 9$ point measurements for each device configuration **b**, Bar graph showcasing the normalized photocurrents on the edge, centre and corner points. Data are expressed as mean ± s.d. derived from measurements of four independent samples ($N = 4$) for each Si-based device configuration. $N = 16$ data points were included for corner and edge plot owing to the fourfold multiplication of locations. PIN-Si and Por-Si show high photocurrent precision, with uniform photocurrents on various device locations.

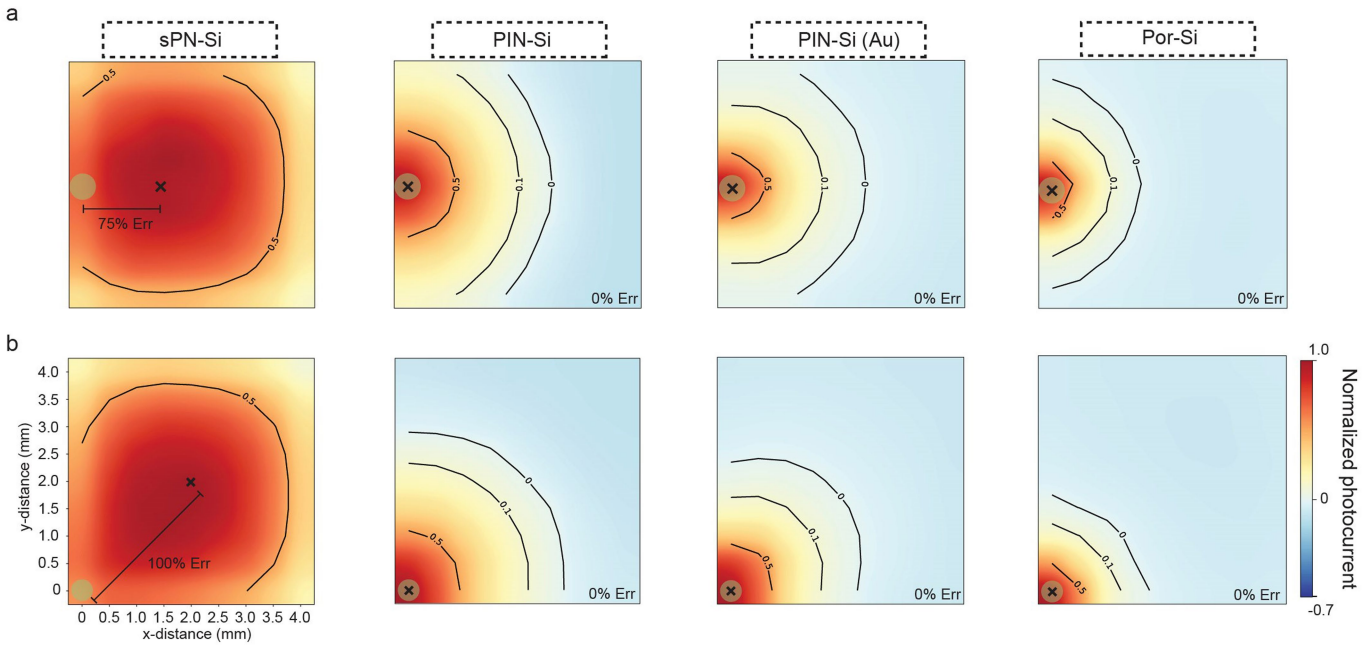

Extended Data Fig. 2 | Characterization of photocurrent accuracy for the four Si-based devices. Accuracy is evaluated by mapping the photocurrent profile on the monolithic device to determine photocurrent magnitude and polarity distributions relative to the illumination spot (centre). We calculate how accurately the photocurrent hotspot aligns with stimulation location. Green dot indicates light spot and location. Black cross represents photocurrent maximum. Error (Err) defines the extent to which the photocurrent maximum deviates from the illumination centre. **a**, sPN-Si showed a 75% error in edge illumination. **b**, sPN-Si showed a 100% error in corner illumination. Detailed calculations can be found in Methods.

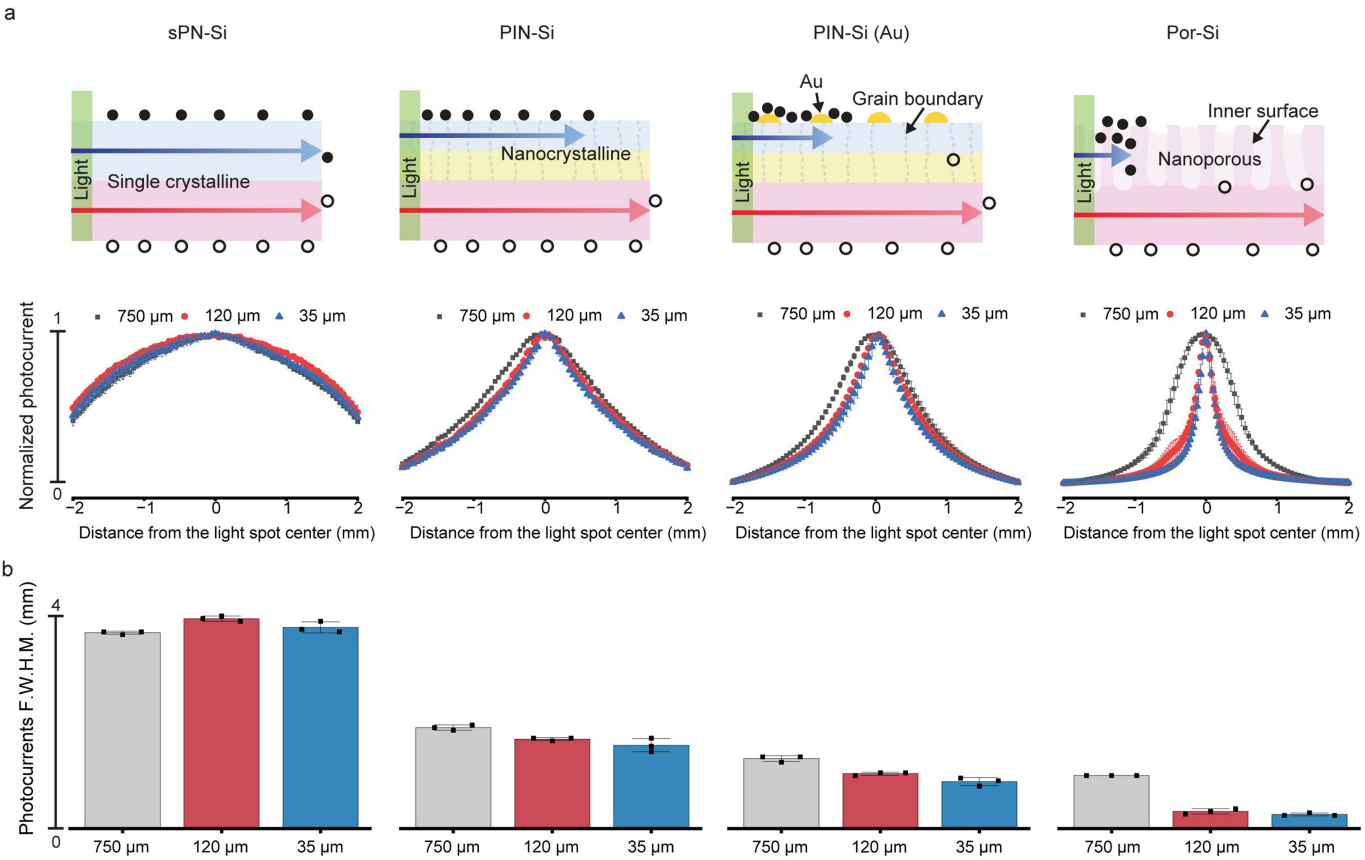

Extended Data Fig. 3 | Further characterizations on photocurrent localization profiles. a, Normalized photocurrent profiles of various Si-based devices under different light-stimulation spot sizes. Data are expressed as mean ± s.d. of $N = 3$ independent samples for each spot size and device configuration. **b**, Photocurrents at FWHM for different spot sizes. Data are expressed as mean ± s.d. of $N = 3$ independent samples for each spot size and device configuration. The Por-Si device showcases superior photocurrent resolution and a tunable FWHM in response to changes in light-spot size.

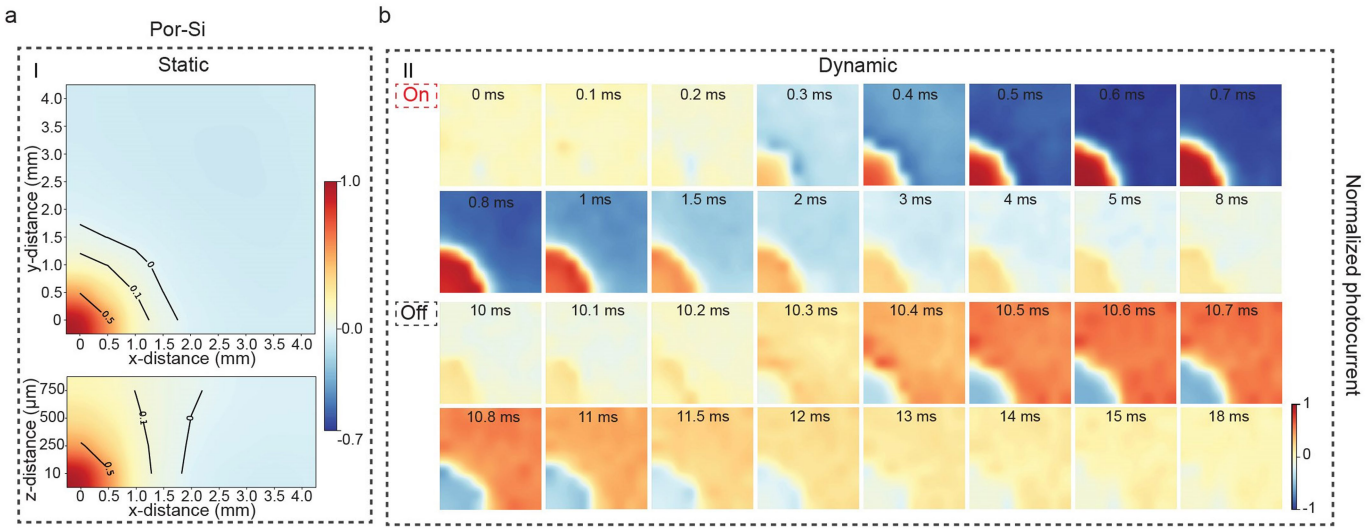

Extended Data Fig. 4 | Static and dynamic spatiotemporal photocurrent profiles of the four devices. a, Two static heat maps demonstrating the photocurrent distribution of Por-Si on horizontal and vertical planes. **b**, Spatiotemporal photocurrent heat maps of monolithic Por-Si reveal bipolarity evolution and domain boundary diffusion during charge (light on) and discharge (light off) when illumination is directed to the device bottom-left corner. The photocurrent normalization methods are different for the static and dynamic profiles (see Methods).

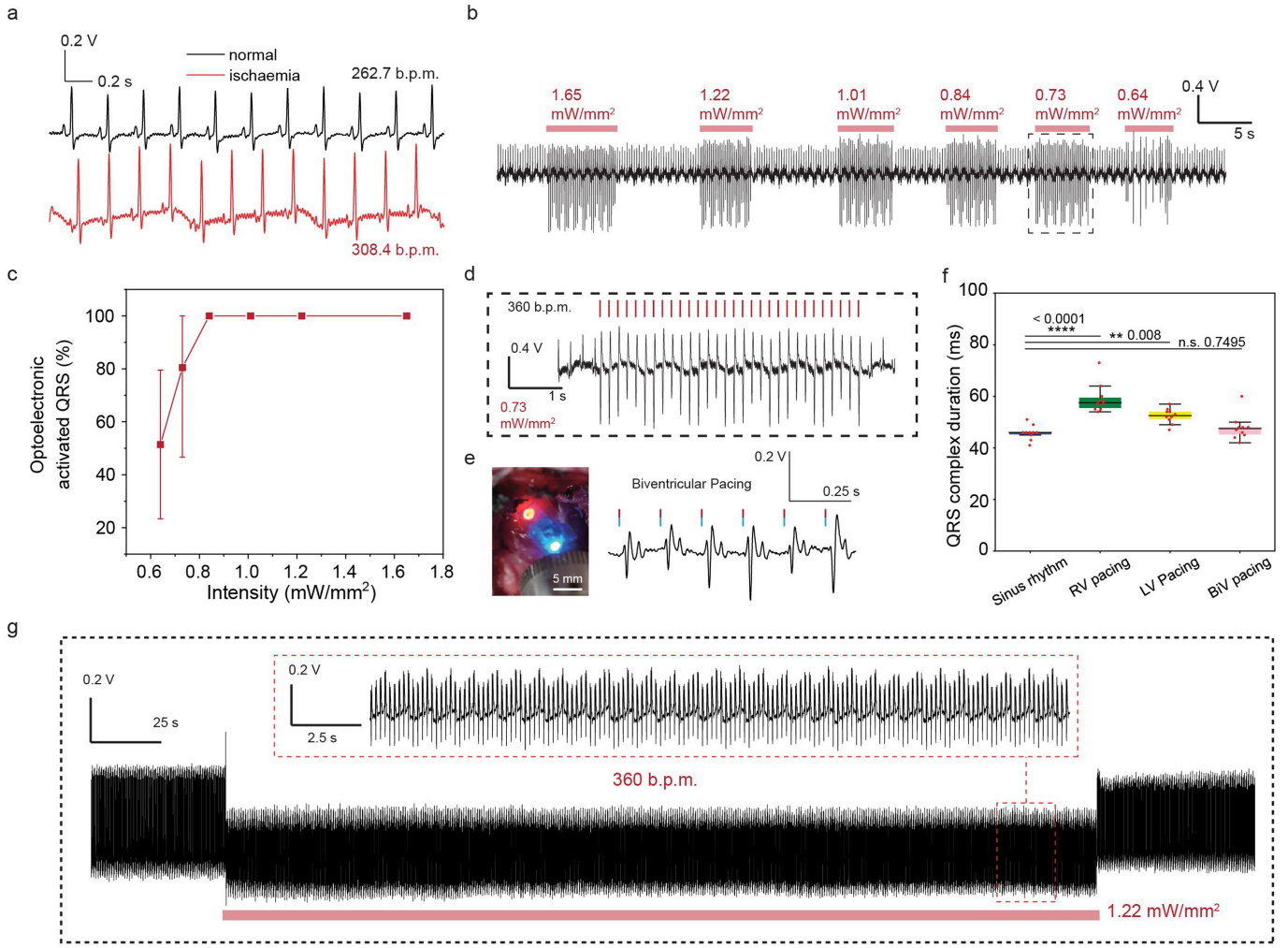

Extended Data Fig. 5 | Further in vivo ischaemic rat heart pacing with 10-ms light pulse duration. a, Plot of ECG waveforms before and after LAD ligation. Acute heart ischaemia results in increased heart rate and stronger breathing cycles, indicated by periodic fluctuations of the baseline. **b**, Optoelectronic pacing on LAD-ligated heart with varying light intensities. Pacing frequency was 360 bpm and pulse duration was 10 ms. Plotted are representative data from $N > 3$ individual rat hearts. **c**, Photostimulation success rate at different intensities. 100% reliability was achieved for intensities above 0.84 mW mm^{-2}. Data are expressed as mean ± s.d. measured from $N = 3$ independent rats and devices. For six the plotted intensities from 0.64 to 1.65 mW mm^{-2}, the total number of QRS evaluated are as follows, respectively: 78, 90, 94, 89, 95 and 95. **d**, Stable and consistent synchronization was demonstrated at 0.73 mW mm^{-2} with 10-ms light duration. Plotted are representative data from $N = 4$ individual rat hearts. **e**, Photograph of biventricular photostimulation on a single monolithic Si device using two spatially separated laser sources with wavelengths of 635 nm and 473 nm. ECG traces show biventricular pacing following simultaneous optoelectronic pacing on the left and right ventricles. **f**, Comparison of QRS durations among sinus rhythm and various pacing conditions. $N = 10$ QRS durations were evaluated for each condition. Boxes bind the IQR divided by the median; whiskers extend 1.5 times the IQR. Statistics are calculated using one-way analysis of variance followed by post hoc Tukey's honestly significant difference test. n.s. > 0.05. $^{**}P < 0.01$, $^{****}P < 0.0001$. **g**, Rat heart optoelectronic pacing at 1.22 mW mm^{-2} for 5 min (approximately 1,800 paced QRS complexes) demonstrated a 100% success rate. Surface ECG data were recorded using an Arduino Uno board and the ECG sensor AD8232.

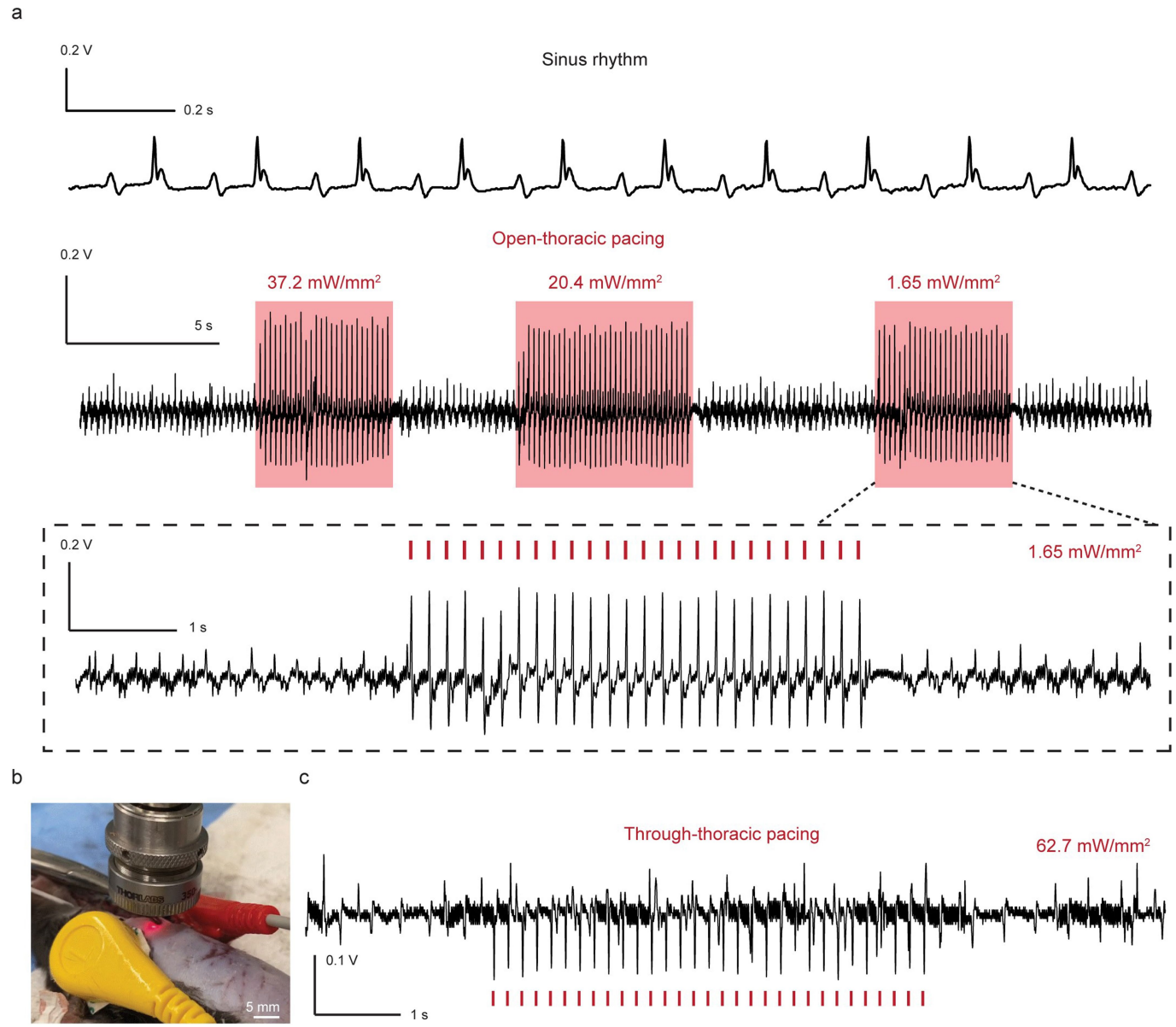

Extended Data Fig. 6 | Optical pacing of in vivo mouse heart. a, Open-thoracic pacing of mouse heart using a 10-ms pulse duration, achieving stable pacing at 360 bpm with optical intensities of 1.65 mW mm^{-2}. **b**, Photograph illustrating the through-thoracic pacing of a mouse heart. **c**, Successful through-thoracic pacing at 360 bpm using optical intensities of 62.7 mW mm^{-2} and a 10-ms pulse duration. $N = 1$ mouse heart experiment was conducted. Mouse surface ECG signals were captured using an Arduino Uno board paired with the ECG sensor AD8232.

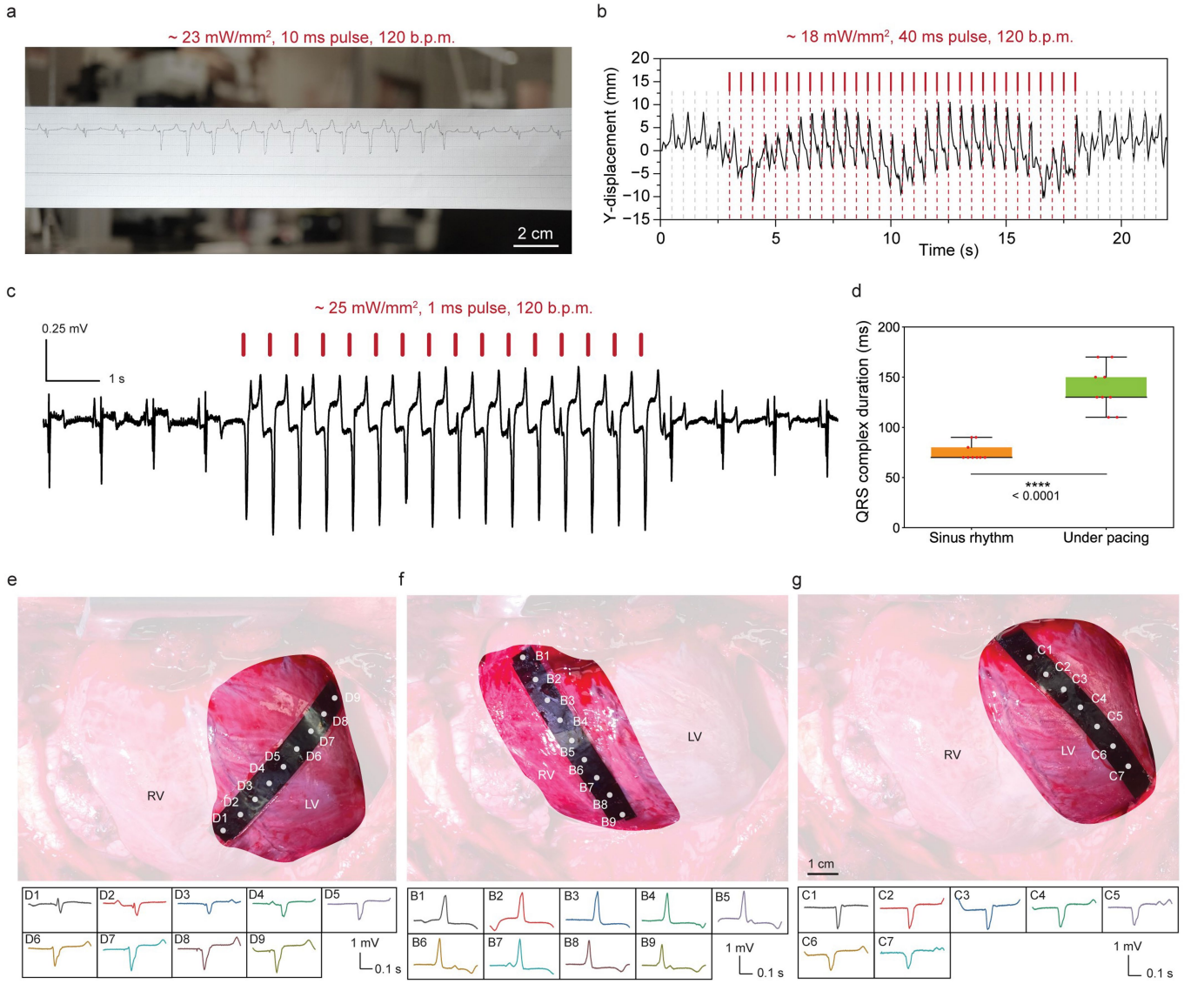

Extended Data Fig. 7 | Further data on in vivo optical pacing of pig heart. **a**, ECG grid paper illustrating the transition from normal to photostimulated ECG waveforms using 23 mW mm^{-2} intensity and 10-ms pulse. **b**, Heart-contraction events depicted as vertical displacement, synchronized with photostimulation at 120 bpm, 18 mW mm^{-2} and 40-ms pulse. **c**, Deterministic pig heart optical pacing at 120 bpm using 1-ms pulse and 25 mW mm^{-2} intensity. **d**, Comparison of photostimulated ECG waveforms with sinus rhythm, showing elongated QRS durations. Statistics was performed using a two-tailed independent-sample *t*-test. ****$P < 0.0001$. Box plots represent IQR divided by the median, with whiskers extending to 1.5 times the IQR from nine analysed waveforms. $N = 9$ QRS waveforms obtained from the same pig experiments were analysed. **e**–**g**, Multisite spatial modulation of pig heart tissues: horizontally on the left ventricle (**e**); longitudinally on the right ventricle (**f**); longitudinally on the left ventricle (**g**). All multisite modulations used 25 mW mm^{-2} intensity and 1-ms pulse duration. To improve the image clarity and remove sensitive content, an artificial white background was incorporated into images **e**–**g**.

nature portfolio

Corresponding author(s): Bozhi Tian, Narutoshi Hibino

Last updated by author(s): Dec 8, 2023

Reporting Summary

Nature Portfolio wishes to improve the reproducibility of the work that we publish. This form provides structure for consistency and transparency in reporting. For further information on Nature Portfolio policies, see our Editorial Policies and the Editorial Policy Checklist.

Statistics

For all statistical analyses, confirm that the following items are present in the figure legend, table legend, main text, or Methods section.

n/a	Confirmed
☐	☒ The exact sample size (*n*) for each experimental group/condition, given as a discrete number and unit of measurement
☐	☒ A statement on whether measurements were taken from distinct samples or whether the same sample was measured repeatedly
☐	☒ The statistical test(s) used AND whether they are one- or two-sided *Only common tests should be described solely by name; describe more complex techniques in the Methods section.*
☒	☐ A description of all covariates tested
☐	☒ A description of any assumptions or corrections, such as tests of normality and adjustment for multiple comparisons
☐	☒ A full description of the statistical parameters including central tendency (e.g. means) or other basic estimates (e.g. regression coefficient) AND variation (e.g. standard deviation) or associated estimates of uncertainty (e.g. confidence intervals)
☐	☒ For null hypothesis testing, the test statistic (e.g. *F*, *t*, *r*) with confidence intervals, effect sizes, degrees of freedom and *P* value noted *Give P values as exact values whenever suitable.*
☒	☐ For Bayesian analysis, information on the choice of priors and Markov chain Monte Carlo settings
☒	☐ For hierarchical and complex designs, identification of the appropriate level for tests and full reporting of outcomes
☒	☐ Estimates of effect sizes (e.g. Cohen's *d*, Pearson's *r*), indicating how they were calculated

Our web collection on statistics for biologists contains articles on many of the points above.

Software and code

Policy information about availability of computer code

Data collection

No custom software was used to perform data collection and manufacturer software was generally used.
DigiData 1550 digitizer was controlled using Clampex software (v. 10.4.0.36, Molecular Devices).
Intantech RHD USB interface board was controlled using RHX software (v. 3.0.4, Intantech).
Tera Term (version 4.106) was used for extracting rat and mouse surface ECG recording from Arduino Uno board.
Nikon inverted microscope Ti2-E and NIS-Elements software (5.30.02) were used to image and record the in vitro experiments.
Videos and images of heart pacing were taken by Sony α6100 camera with a 30mm macro lens (E 3.5/30, Sony)
Endoscopic images were collected by commercial endoscope (Oiiwak, Amazon Standard Identification Number: B07SXR6TF6)

Data analysis	Standard photocurrent measurement and analysis was performed with Python (v. 3.9.16) scripts using Numpy (v. 1.19.5), Matplotlib (3.6.2). ABF files were opened using pyabf (v. 2.3.7). Statistics was calculated using stats modules in Scipy (v. 1.10.1) to perform two-tailed t tests, pair T test and one way anova. Statsmodels (0.13.5) was used for performing Tukey's HSD test. For imaging and videos processing, python tifffile (2021.4.8), Matplotlib (3.6.2), Scipy version 1.10.1 and ImageJ (1.8.0_345) were used. Epicardial recordings from Intantech files were performed with python (v. 3.9.16) scripts using Numpy (v. 1.19.5), Matplotlib (3.6.2), Pandas (v. 1.4.4). Box plots were performed with python (v. 3.9.16) scripts using Numpy (v. 1.19.5), Matplotlib (3.6.2). Adobe Premiere Pro (v. 23.4.0) was used for cropping and slicing video recordings. Pig heart movement analysis was performed using ImageJ (v. 1.8.0_345). Photomasks were designed in AutoCAD 2023 (v. T.53.0.0). OriginPro 2023b (10.0.5.157) and Matplotlib (3.6.2) was used to plot the graphs. Gatan DigitalMicrograph (3.52.3932.0) was used to access and process transmission electron microscope data.

For manuscripts utilizing custom algorithms or software that are central to the research but not yet described in published literature, software must be made available to editors and reviewers. We strongly encourage code deposition in a community repository (e.g. GitHub). See the Nature Portfolio guidelines for submitting code & software for further information.

Data

Policy information about availability of data

All manuscripts must include a data availability statement. This statement should provide the following information, where applicable:

- Accession codes, unique identifiers, or web links for publicly available datasets
- A description of any restrictions on data availability
- For clinical datasets or third party data, please ensure that the statement adheres to our policy

The research findings presented in this study are substantiated by the data included within the main body of the article as well as its Supplementary Information. The source data and raw data have been made publicly accessible through the link: https://osf.io/kr67g/

Research involving human participants, their data, or biological material

Policy information about studies with human participants or human data. See also policy information about sex, gender (identity/presentation), and sexual orientation and race, ethnicity and racism.

Reporting on sex and gender	N/A
Reporting on race, ethnicity, or other socially relevant groupings	N/A
Population characteristics	N/A
Recruitment	N/A
Ethics oversight	N/A

Note that full information on the approval of the study protocol must also be provided in the manuscript.

Field-specific reporting

Please select the one below that is the best fit for your research. If you are not sure, read the appropriate sections before making your selection.

☒ Life sciences ☐ Behavioural & social sciences ☐ Ecological, evolutionary & environmental sciences

For a reference copy of the document with all sections, see nature.com/documents/nr-reporting-summary-flat.pdf

Life sciences study design

All studies must disclose on these points even when the disclosure is negative.

Sample size	For absolute photocurrent magnitude measurement for each device type, N = 8 independent devices was chosen for each device type to account for variability in material preparation. N = 4 was used for photocurrent precision measurement, N = 3 was used for photocurrent mapping and resolution profile plotting. For cell photostimulation, N = 8 stimulation events were performed for evaluating the excited cellular area. For quantitative calcium studies, N = 6 different cells were used. For gene analysis with RT-QPCR, N = 5 replications were performed. For in vivo pig experiment, N = 3 pigs were used in this study. Sample size for photostimulation of tissues was not predefined. Samples size was determined based on the laboratory experience and was deemed to be sufficient to demonstrate representative effects of photostimulation. Positive effect is observed for successfully processed devices and no effect is observed otherwise. Therefore increase in the sample size does not further increase the power of statistical analysis.

Data exclusions	In Supplementary Fig. 33., one set of parallel data points for Nrf1 with all 6 conditions were excluded, due to its unreasonable deviation from the normal values. Since the outlier appears in all 6 conditions, we rationally assume it to be bad sample preparations on the same testing row or column. This exclusion is not due to natural sample variance but issues in sample preparation. For other plots in the manuscript, no other data were excluded.
Replication	In vitro cell stimulation results are representatives of over three independent cell culture dishes and devices. Ex vivo heart stimulation results are representative of over three independent experiments performed with different membranes and hearts. In vivo rat heart stimulation results are representative of over three independent experiments with different devices and rats. In vivo pig heart experiment results are representative of two independent experiments with different devices and pigs. All experimental replicates were successful with properly prepared devices.
Randomization	No randomization was performed. Single effect type (photoelectrochemical stimulation) was evaluated and no known co-variates exist for such experiment. The experimental subjects were drawn from homogeneous population of laboratory animals with same gender, similar ages and body weights. No significant variability in response to photostimulation is expected. No stimulation was observed with light alone. Deterministic stimulation was achieved when the optical power is above the threshold.
Blinding	The first author performed all material preparation and photostimulation, therefore no additional staff was available to perform blinded investigations in animal experiments. Photocurrent analysis was performed using numerical methods, therefore experimenter blinding does not contribute bias to the analysis.

Reporting for specific materials, systems and methods

We require information from authors about some types of materials, experimental systems and methods used in many studies. Here, indicate whether each material, system or method listed is relevant to your study. If you are not sure if a list item applies to your research, read the appropriate section before selecting a response.

Materials & experimental systems

n/a	Involved in the study
☐	☒ Antibodies
☒	☐ Eukaryotic cell lines
☒	☐ Palaeontology and archaeology
☐	☒ Animals and other organisms
☒	☐ Clinical data
☒	☐ Dual use research of concern
☒	☐ Plants

Methods

n/a	Involved in the study
☒	☐ ChIP-seq
☒	☐ Flow cytometry
☒	☐ MRI-based neuroimaging

Antibodies

Antibodies used	BD Pharmingen™ Alexa Fluor® 647 Mouse Anti-Cardiac Troponin T (BD Biosciences 565744)
Validation	https://www.bdbiosciences.com/en-us/products/reagents/flow-cytometry-reagents/research-reagents/single-color-antibodies-ruo/alexa-fluor-647-mouse-anti-cardiac-troponin-t.565744#:~:text=Cardiac%20Troponin%20T%20can%20be,derived%20from%20pluripotent%20stem%20cells.&text=Alexa%20Fluor%E2%84%A2%20647%20Dye,Max)%20at%20669%2Dnm.

Animals and other research organisms

Policy information about studies involving animals; ARRIVE guidelines recommended for reporting animal research, and Sex and Gender in Research

Laboratory animals	CD/SD rats were originally obtained from Charles River and were housed and bred in the animal facility at the University of Chicago; C57BL/6J mice (6 – 8 weeks) were purchased from JAX; Female crossbred swine obtained from a USDA Class A vendor.
Wild animals	No wild animals were used in the study
Reporting on sex	We utilize male rats for our ex vivo and in vivo heart experiments to maintain consistency in heart size. The sex of mice was not specified. We utilized female swine for in vivo pig heart experiment.
Field-collected samples	No field collected samples were used in the study
Ethics oversight	All animal procedures were approved by the Institutional Animal Care and Use Committee of the University of Chicago in protocol number 72378, 72523, and 72605.

Note that full information on the approval of the study protocol must also be provided in the manuscript.